# Earthquake swarms frozen in an exhumed hydrothermal system (Bolfin Fault Zone, Chile)

Simone Masoch[1*], Giorgio Pennacchioni[1], Michele Fondriest[1], Rodrigo Gomila[1], Piero Poli[1], José Cembrano[2,3], Giulio Di Toro[1,4]

*1. Dipartimento di Geoscienze, Università degli Studi di Padova, Padua, ITALY*

*2. Departamento de Ingeniería Estructural y Geotécnica, Pontificia Universidad Católica de Chile, Santiago, CHILE*

*3. Andean Geothermal Center of Excellence (CEGA, FONDAP-CONICYT), Santiago, CHILE*

*4. Sezione di Tettonofisica e Sismologia, Istituto Nazionale di Geofisica e Vulcanologia, Rome, ITALY*

[*] corresponding author: Simone Masoch simone.masoch@phd.unipd.it

## Key Points

- Epidote-rich veins exhumed from 3-5 km depth are well-exposed in the Atacama Desert and fill honey mesh-like fault-fracture networks.
- Wall-rock microstructures record rupture propagation; instead, fault-veins record cyclic veining and aseismic-seismic shearing.
- The epidote-rich fault-vein networks represent ancient seismogenic hydrothermal systems, possibly producing earthquake swarms.

**Abstract**

Earthquake swarms commonly occur in upper-crustal hydrothermal-magmatic systems and activate mesh-like fault-fracture networks at zone of fault complexity. How these networks develop through space and time along seismic faults is poorly constrained in the geological record. Here, we describe a spatially dense array of small-displacement (< 1.5 m) epidote-rich fault-veins within granitoids, occurring at the intersections of subsidiary faults with the exhumed seismogenic Bolfin Fault Zone (Atacama Fault System, Northern Chile). Epidote faulting and veining occurred at 3-7 km depth and 200-300 °C ambient temperature. At distance ≤ 1 cm to fault-veins, the magmatic quartz of the wall-rock shows (i) thin (<10-µm-thick) interlaced deformation lamellae, and (ii) crosscutting quartz-healed veinlets. The epidote-rich fault-veins (i) include clasts of deformed magmatic quartz, with deformation lamellae and quartz-healed veinlets, and (ii) record cyclic events of extensional-to-hybrid veining and either aseismic and seismic shearing. Deformation of the wall-rock quartz is interpreted to record the large stress perturbations associated with the rupture propagation of small earthquakes. Instead, dilation and shearing forming the epidote-rich fault-veins are interpreted to record the later development of a mature and hydraulically-connected fault-fracture system. In this latter stage, the fault-fracture system cyclically ruptured due to fluid pressure fluctuations, possibly correlated with swarm-like earthquake sequences.

**Keywords:** earthquake swarm, fault zone, seismically-active fault-fracture network, veining, deformation lamellae.

## 1. Introduction

The thermo-hydro-mechanical and chemical properties of fault zones and their host rocks affect a wide range of processes in the Earth's crust, such as earthquake nucleation, propagation and arrest (e.g., Faulkner et al., 2006; Sibson, 1985; Wesnousky, 1988, 2006), crustal rheology (e.g., Behr & Platt, 2014; Handy et al., 2007) and migration of fluids (e.g., hydrothermal, magmatic, oil, gas; Cembrano & Lara, 2009; Mittempergher et al., 2014; Richards, 2013; Tardani et al., 2016). The mechanical and hydraulic proprieties of fault zones vary largely through space and time during the seismic cycle and are intrinsically coupled (Caine et al., 1996; Faulkner et al., 2010; Wibberley et al., 2008). In particular, permeability changes during the seismic cycle at seismogenic depths are expected to promote co- to post-seismic episodic fluid flow (i.e., fault-valve behavior; Sibson, 1989, 1992a, 1992b). Indeed, fault rupture events can lead to large, transitory increases of fault permeability (Cox, 2016; Sibson, 1989). Where ruptures breach overpressured fluid reservoirs, high-permeability fault segments provide conduits facilitating fluid redistribution in the Earth's crust. On the other hand, post- to inter-seismic fault healing and sealing due to compaction and precipitation of hydrothermal minerals in pores and fractures reduce fault permeability, eventually arresting fluid flow (Cox, 2016; Sibson, 1989, 1992b, 1992a).

The expression of the coupling among fault activity, fault permeability, fluid flow, fluid pressure and loading conditions in the geological record is documented by hydrothermal (e.g., epidote, quartz, chlorite, calcite, zeolite) fault-vein networks in exhumed fault zones over several geological settings (e.g., Cerchiari et al., 2020; Cox & Munroe, 2016; Dempsey et al., 2014; Lucca et al., 2019; Malatesta et al., 2021; Masoch et al., 2022; Micklethwaite et al., 2010; Ujiie et al., 2018). Mineralized fault-fracture networks display extensive hydrothermal alteration, mutually overprinting extension-to-hybrid vein arrays and dilatant breccias (Cox, 2016; Sibson, 2020). These features record significant stages of fluid flow and mineral precipitation during fault evolution, possibly associated with ancient seismic activity (e.g., Boullier & Robert, 1992; Cox, 2020; Cox & Munroe, 2016; Dempsey et al., 2014; Genna et al.,

1996; Micklethwaite & Cox, 2004; Muñoz-Montecinos et al., 2020; Ujiie et al., 2018). In recently or currently active hydrothermal-magmatic settings, abundant fluid flow is commonly accompanied by earthquake swarms (e.g., Danré et al., 2022; Enescu et al., 2009; Fischer et al., 2014; Legrand et al., 2011; Mesimeri et al., 2021; Passarelli et al., 2018; Shelly et al., 2016; 2013; Yukutake et al., 2011), i.e., clusters of low magnitude seismic events without a characteristic mainshock (Mogi, 1963). Earthquake swarm events, lasting from a few days to months (e.g., Fischer et al., 2014), are driven by either pore fluid pressure fluctuations (e.g., Baques et al., 2023; Hill, 1977; Ross & Cochran, 2021; Shelly et al., 2022; Sibson, 1996) and aseismic slip (e.g., Danré et al., 2022; De Barros et al., 2020; Lohman & McGuire, 2007; Vidale & Shearer, 2006). Besides deviating from common mainshock-aftershock sequences, earthquake swarms generate also considerable non-double-couple (i.e., isotropic) seismic signal, as a result of tensile fracturing and hybrid faulting attributed to the ingression of pressurized fluids in the fault zone/system (Legrand et al., 2011; Phillips, 1972; Sibson, 1996; Stierle et al., 2014; Vavryčuk, 2002). Similar human-induced seismic sequences may be associated with industrial fluid injection in boreholes (e.g., Ellsworth, 2013; Goebel et al., 2016; Guglielmi et al., 2015; Healy et al., 1968).

There has been a great deal of progress in the last years regarding (i) the imaging of fault networks illuminated by earthquake swarms (e.g., Baques et al., 2023; Ross et al., 2020; Shelly et al., 2022), (ii) the determination of focal mechanisms of very small-in-magnitude earthquakes through seismological analysis (e.g., Essing & Poli, 2022; Mesimeri et al., 2021; Poli et al., 2021), and (iii) the relation of injected fluid volumes and rates with seismic energy release through fluid-injection experiments (e.g., Dorbath et al., 2009; Guglielmi et al., 2015; McGarr, 2014). Many authors proposed that swarm-like earthquake sequences activate km-scale mesh-like fault-fracture networks in zones of fault geometric complexity, such as fault linkages and step-overs (e.g., Hill, 1977; Ross et al., 2020; Ross et al., 2017; Shelly et al., 2022, 2015; Sibson, 1996; Sykes, 1978). However, to date, how a fault-fracture network develops both in space and time in seismically-active hydrothermal systems is poorly constrained due to

(i) the poor spatial resolution (> 10s of meters) of seismological and geophysical techniques relative to the length of (micro-)fracture processes and (ii) the limited exposure at the Earth's surface of exhumed fault-vein networks large enough to be comparable to currently active cases.

In this work, we examine an extensive epidote-rich fault-vein network located at a linkage zone of the Bolfin Fault Zone (BFZ), well-exposed at centimeter-to-decameter scales over tens of square kilometers in the Atacama Desert (Northern Chile). The BFZ is an exhumed, crustal-scale, seismogenic (pseudotachylyte-bearing) fault of the transtensional Coloso Duplex (Atacama Fault System, Chile, Figure 1) (Cembrano et al., 2005; Masoch et al., 2022, 2021; Scheuber & González, 1999). Based on the interpretation of field data and high-resolution (FEG-SEM) microstructural analysis of fault zone rocks, we reconstruct different stages during the development of an upper-crustal seismically-active hydrothermal system. The proximal wall-rock of small-displacement (< 1.5 m) fault-veins initially experienced a large transient stress pulse, attested by the occurrence of deformation lamellae within magmatic quartz. This deformed quartz is included as clasts within epidote-rich fault-veins, that record overprinting events of extensional veining and cataclasis. We interpret these microstructures as evidence of ancient swarm-like activity, from the first stages of dynamic crack propagation to the later cyclic crack opening and both seismic or aseismic slip, driven by fluid pressure fluctuations, within a mature and hydraulically connected fault-fracture system. These exposed fault-vein networks represent a unique geological record of the evolution in space and time of upper-crustal swarm-like seismic sources, from the early nucleation stage to the later development of a mature fault system.

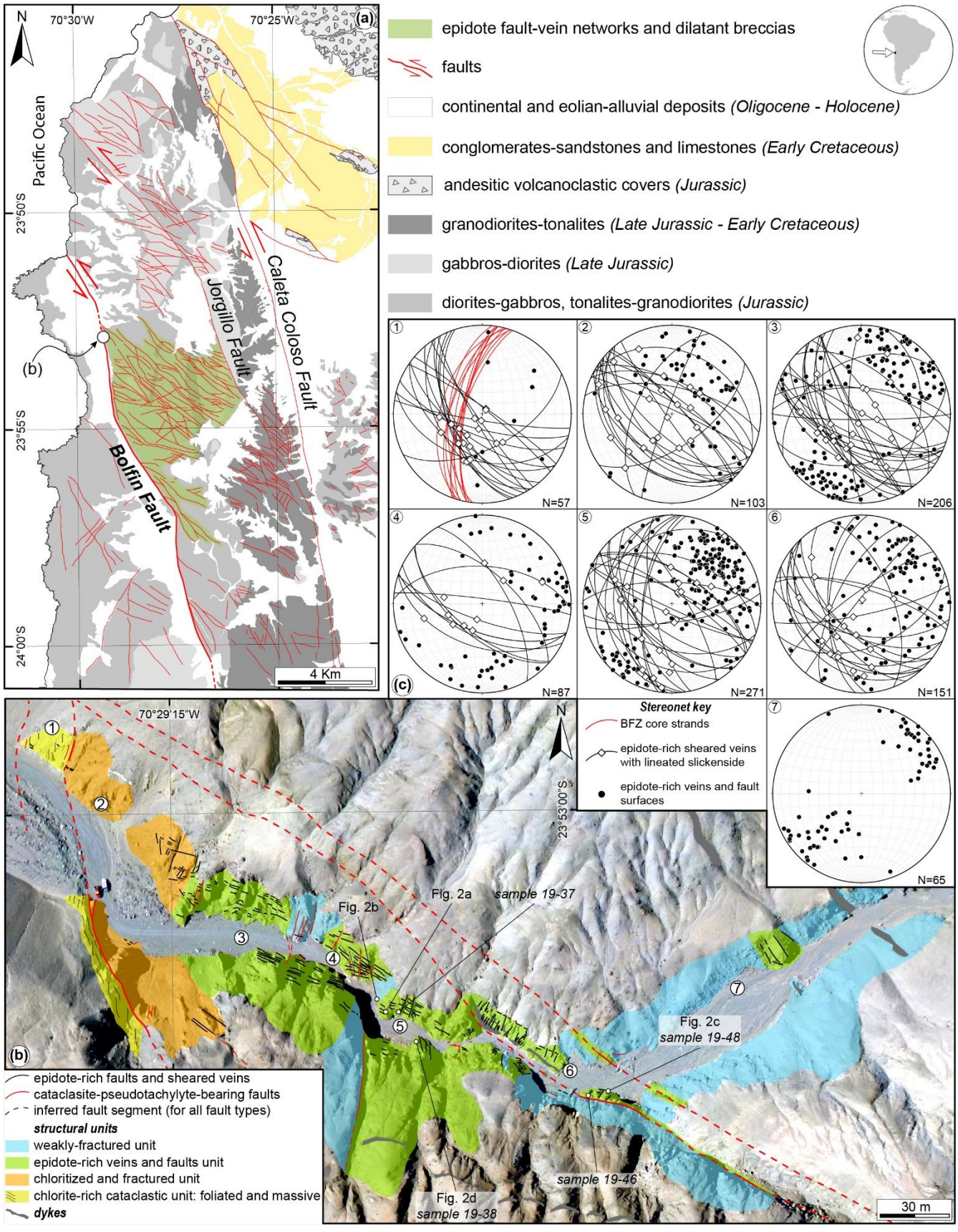
N
70°30'W
70°25'W
(a)
Pacific Ocean
23°50'S
23°55'S
24°00'S
Jorgillo Fault
Caleta Coloso Fault
Bolfin Fault
(b)
4 Km
epidote fault-vein networks and dilatant breccias
faults
continental and eolian-alluvial deposits (Oligocene - Holocene)
conglomerates-sandstones and limestones (Early Cretaceous)
andesitic volcanoclastic covers (Jurassic)
granodiorites-tonalites (Late Jurassic - Early Cretaceous)
gabbros-diorites (Late Jurassic)
diorites-gabbros, tonalites-granodiorites (Jurassic)
N=57
N=103
N=206
N=87
N=271
N=151
N=65
(c)
Stereonet key
BFZ core strands
epidote-rich sheared veins with lineated slickenside
epidote-rich veins and fault surfaces
70°29'15"W
23°53'00"S
Fig. 2a
sample 19-37
Fig. 2b
Fig. 2c
sample 19-48
Fig. 2d
sample 19-38
sample 19-46
30 m
epidote-rich faults and sheared veins
cataclasite-pseudotachylyte-bearing faults
inferred fault segment (for all fault types)
structural units
weakly-fractured unit
epidote-rich veins and faults unit
chloritized and fractured unit
chlorite-rich cataclastic unit: foliated and massive
dykes

**Figure 1.** Geological setting of the Bolfin Fault Zone. (a) Simplified geological map of the Coloso Duplex. The BFZ bounds the western side of the crustal-scale transtensional duplex. The green area indicates the distribution of the epidote-rich fault-vein networks and dilatant breccias within the Coloso Duplex. Modified from Cembrano et al. (2005). (b) Structural map of the BFZ architecture at Sand Quarry locality. Clusters of epidote-rich fault-vein networks and breccias are associated with NW-striking, splay faults of the BFZ, and NE-striking faults. The faults splaying out from the BFZ represent transtensional faults within the duplex (thick red lines). Modified from Masoch et al. (2022). (c) Structural data of the fault core strands and epidote-rich fault-vein networks. Numbers in stereonets denote the location of structural sites in the map in (b).

## 2. The epidote-rich fault-vein networks of the Bolfin Fault Zone

The >40-km-long BFZ pertains to the 1000-km-long, Early Cretaceous, strike-slip intra-arc Atacama Fault System (Northern Chile; Figure 1) (Arabasz, 1971; Cembrano et al., 2005; Masoch et al., 2021; Scheuber & González, 1999; Seymour et al., 2021). The BFZ displays sinistral strike-slip kinematics and bounds the western side of the crustal-scale transtensional Coloso Duplex (Cembrano et al., 2005; Masoch et al., 2022, 2021) (Figure 1a). At regional scale, the BFZ has a sinuous geometry across Jurassic-Early Cretaceous diorite-gabbro and tonalite-granodiorite plutons (Figure 1a). The ancient (125-118 Ma) BFZ seismicity is attested by presence of pseudotachylytes, formed at 5-7 km depth and ≤ 300 °C ambient temperature (Gomila et al., 2021; Masoch et al., 2022, 2021). Seismic faulting occurred in a fluid-rich environment as documented by syn-kinematic chlorite-epidote (-quartz-calcite) veining and extensive propylitic alteration (Gomila et al. 2021).

In detail, the BFZ architecture consists of multiple (ultra)cataclastic strands, up 6-m-thick, within a 150-m-wide damage zone (see Masoch et al., 2022 for the description of the fault architecture; Figure 1b). The damage zone consists of variably fractured and brecciated rock volumes characterized by extensive epidote-rich fault-vein networks associated with NW-to-WNW-striking faults splaying from the BFZ (Figures 1b-c; 2) (Masoch et al., 2022). These subsidiary faults accommodated transtensional

144 slip (Figure 1c) within the Coloso Duplex (Cembrano et al., 2005; Veloso et al., 2015), with an apparent
145 cumulative strike-slip displacement up to 1 km (Cembrano et al., 2005; Jensen et al., 2011; Stanton-
146 Yonge et al., 2020). The epidote-rich fault-vein networks consist of (i) small-displacement (< 1.5 m)
147 sheared veins with lineated slickensides (Figure 2a-b, 2d-e), and (ii) extensional veins and dilatant
148 breccias sealed by epidote + prehnite ± chlorite ± quartz ± K-feldspar (Figure 2b-c, 2f; see section 4.2).
149 The small-displacement epidote-rich fault-veins extend up to tens of meters in length (Figure 1b).
150 Sheared and extensional veins are arranged in four sets, dipping towards SW, NE, NW and S (Figure
151 1c). Epidote lineated slickensides are decorated by either stepped polished surfaces or mirror-like slip
152 surfaces (Figure 2a, 2d), and their kinematics range from normal dip-slip to strike-slip (either sinistral
153 and dextral; Figure 1c). Veins and breccias record repeated episodes of extensional fracturing and
154 sealing, as they include angular fragments of earlier veins and breccias (Figure 2b-c). The epidote-rich
155 fault-vein networks are surrounded by extensive reddish alteration haloes in the damaged wall-rock
156 (Figure 2b-c, 2e-f). The epidote-rich fault-vein networks observed in the BFZ damage zone are spatially
157 distributed within all the duplex (see Cembrano et al., 2005; Herrera et al., 2005) (Figure 1a).
158

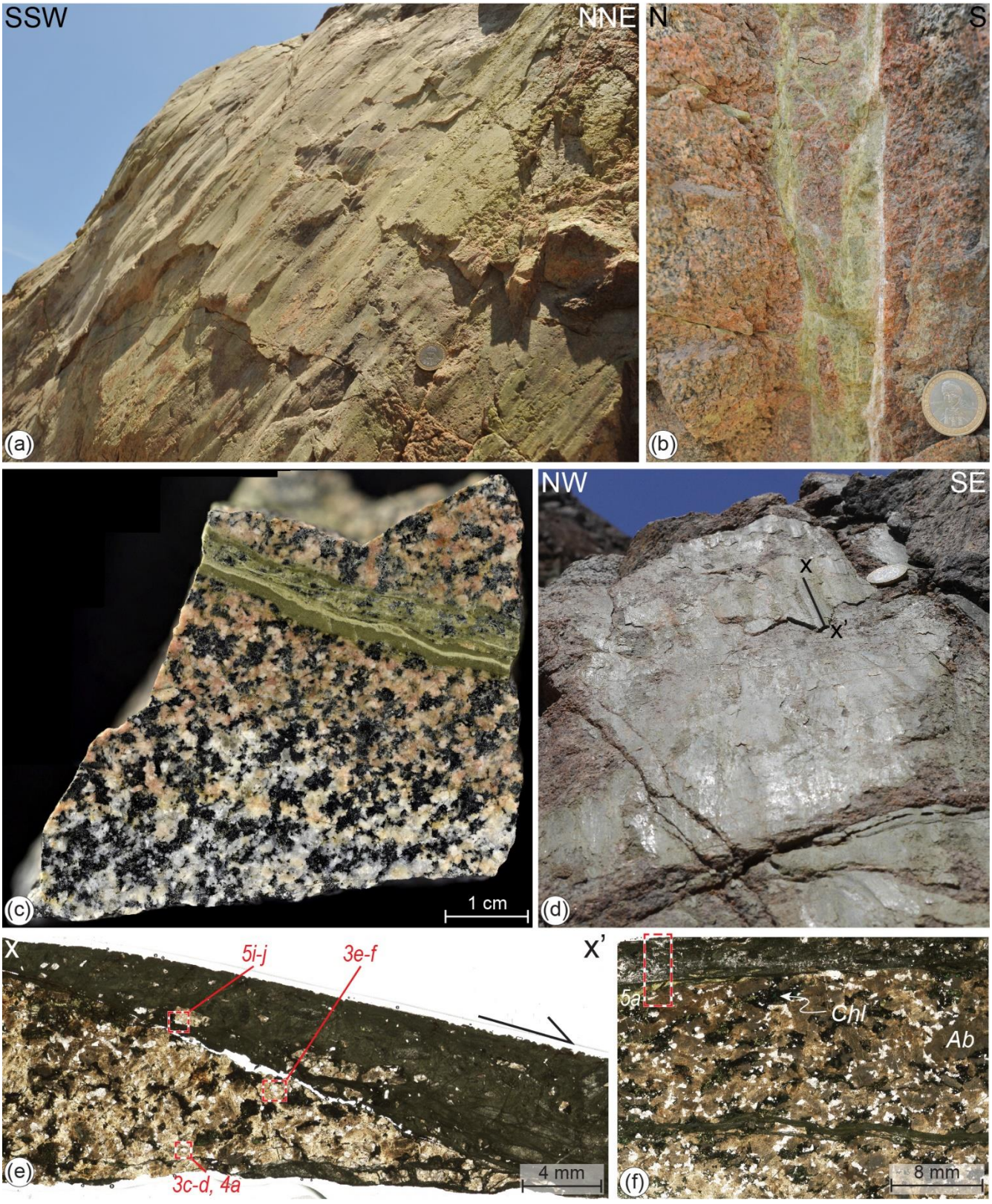


**Figure 2.** The epidote-rich fault-vein network of BFZ. Coin for scale. Mineral abbreviations: *Ab* = albite, *Chl* = chlorite. (a) Discrete extensional fault surface decorated by epidote slickenfibers. WGS84 GPS

location: 23.883944°S, 70.486689°W. Modified from Masoch et al. (2022). (b) Epidote-rich hybrid extensional-shear vein including angular fragments of earlier veins (dark green). The vein is reactivated by a whitish calcite-palygorskite vein (boundary on the right side), referable to post-Miocene deformation (see Masoch et al., 2021 for details). Sample 19-33. WGS GPS location: 23.99803°S, 70.44051°W. Modified from Masoch et al. (2022). (c) Polished sample of an epidote sheared vein surrounded by a reddish alteration halo on both sides. The pale green-colored cataclasite includes dark green fragments of early veins. Sample 19-48. WGS84 GPS location: 23.88442°S, 70.48567°W. Modified from Masoch et al. (2022). (d) Sheared vein with lineated and highly reflective (i.e., mirror-like) slickenside. The black line indicates the orientation of the thin section scan shown in (e). Sample 19-38. WGS84 GPS location 23.88424°S, 70.48642°W. (e) Plane-polarized light scan of thin section of a lineated sheared vein, showing the spatial distribution of the microstructures observed in the micro-damage zone and in the sheared vein (red lines). (f) Plane-polarized light scan of thin section of a sheared vein recording multiple episodes of extensional-to-hybrid veining and along vein-boundary shearing. Sample 19-46. WGS84 GPS location 23.88428°S, 70.48615°W.

## 3. Methods

Microstructural analysis was conducted on Syton-polished 100-µm-thick thin sections (n=10) cut parallel to the fault lineation and orthogonal to the fault/vein wall. We used a Tescan Solaris (Field Emission Gun – Scanning Electron Microscope; FEG-SEM) installed at the Department of Geosciences of University of Padova (Italy). The instrument is equipped with backscattered electron (BSE), cathodoluminescence (CL), electron backscattered diffraction (EBSD), and quantitative wavelength-dispersive spectroscopy (WDS) detectors. BSE and CL images were acquired at 5-10 kV and 0.3-3 nA, and 10 kV and 1-3 nA as accelerating voltage and beam current, respectively. The EBSD maps were acquired using the FEG-SEM equipped with a COMOS-Symmetry EBSD detector (AZtec acquisition software, Oxford Instruments), operating at 20 kV as accelerating voltage, 5-10 nA as beam current, 0.15-0.30 µm as step size, 70° sample tilt and high vacuum. EBSD data were elaborated with the MTEX toolbox (https://mtex-toolbox.github.io/).

189 The composition of main mineral phases was obtained by WDS-FEG analysis. Acquisition
190 conditions were: 15 kV (accelerating voltage); 6 nA (beam current); 1 µm (electron beam size); 5 s
191 (counting time for background), 15 s (for Si, Al, Ca, Fe), and 10 s (for Na, K, Mg, Mn, Ti, Cr) on peak.
192 Albite (Si, Al and Na), diopside (Ca), olivine San Carlos (Mg), orthoclase (K), hematite (Fe), and Cr, Ti
193 and Mn oxides were used as standards. Na and K were analyzed first to prevent alkali migration affects.
194
195 **4. Results**
196 *4.1. Weakly-deformed granodiorite and micro-damage zone of the sheared veins*
197 The weakly-deformed granodiorite consists of plagioclase (labradorite to andesine; Masoch et al.,
198 2022), quartz, K-feldspar with myrmekite, biotite, minor amphibole, ilmenite and magnetite (Figure 2c).
199 The magmatic quartz shows weak undulose extinction and has a dominant bright to light grey CL shade
200 locally cut by CL-dark micro-fractures (>10 µm in thickness) sealed by hydrothermal quartz ± K-feldspar
201 (Figure 3a-b).
202 The granodiorite adjacent to epidote-rich sheared veins is turned into reddish alteration haloes,
203 up to 4 cm in thickness (Figures 2b-f), associated with (i) replacement of magmatic plagioclase by albite
204 + epidote, and of magmatic biotite and amphibole by chlorite ± opaques (Figure 2e-f), (ii) pervasive
205 micro-fracturing, filled with epidote ± chlorite ± prehnite (Figure 2c, 2e-f), and (iii) deformation of the
206 magmatic quartz. Quartz deformation microstructures include interlaced deformation bands, up to 10-
207 µm-thick, visible in CL by the darker shade crosscutting the bright to medium grey-shaded host quartz
208 (Figure 3c-f). The deformation bands are in turn crosscut by thin (up to 15-µm-thick) micro-fractures
209 healed by quartz ± K-feldspar ± albite (hereafter referred as "quartz-filled" veinlets), across quartz and
210 K-feldspar grains (Figure 3c-f). These veinlets show a homogeneous dark CL shade and are oriented at
211 high angle with respect to the vein boundary (Figure 3f). These deformation microstructures (hereafter
212 referred to as "micro-damage zone") fade away from the veins and disappear at distances ≥ 1 cm (Figure

213 3a-b). In the micro-damage zone, the quartz-filled veinlets increase in spatial density towards the veins
214 (Figure 3c-f), while no apparent change in density of deformation bands is observed. In the footwall
215 block, at < 100 μm distance from the sharp vein boundary, the magmatic quartz is strongly brecciated
216 and healed by CL-dark grey-shaded quartz (also surrounded by epitaxial rim of CL-dark quartz; Figure
217 3g-h).

218 EBSD maps of the quartz show that the deformation bands visible in CL are oriented nearly
219 orthogonal to the <c> axis (Figure 4a-b) and correspond to a minor crystallographic misorientation (< 2-
220 3°; see profiles in Figure 4c) with respect to the host grain. These features are typical of deformation
221 lamellae (Fairbairn, 1941; Trepmann & Stöckhert, 2003), either referred to as short-wavelength
222 undulatory extension (Trepmann & Stöckhert, 2013) or fine extinction bands (Derez et al., 2015).
223 Therefore, quartz deformation bands will be referred to hereafter as deformation lamellae. The EBSD
224 maps also show that the quartz-filled veinlets overgrew in epitaxial continuity with the host magmatic
225 quartz (Figure 4a).
226

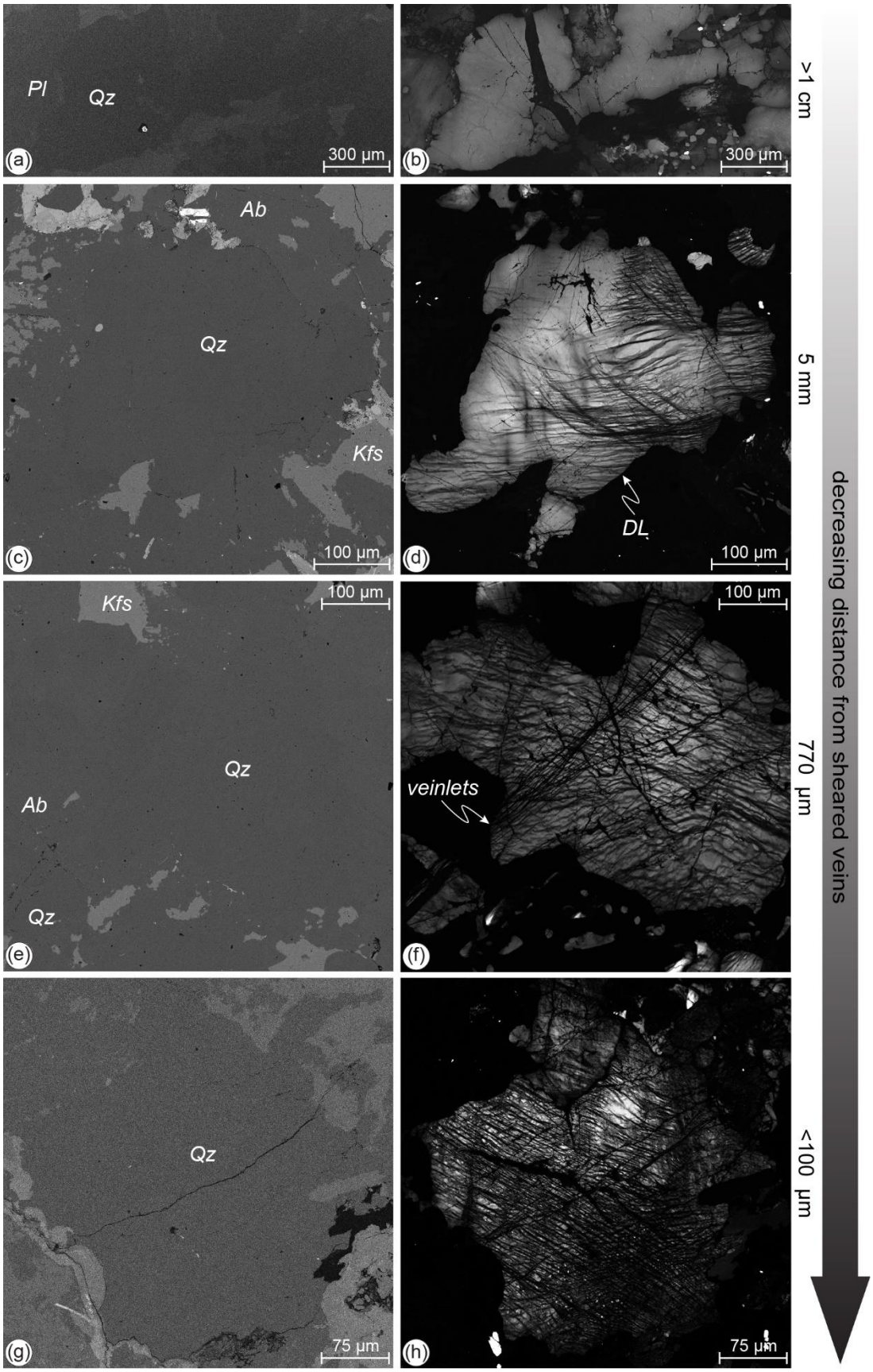
Pl
Qz
(a)
300 µm
(b)
300 µm
>1 cm
Ab
Qz
Kfs
(c)
100 µm
(d)
DL
100 µm
5 mm
Kfs
100 µm
Qz
Ab
Qz
(e)
100 µm
veinlets
(f)
770 µm
Qz
(g)
75 µm
(h)
75 µm
<100 µm
decreasing distance from sheared veins

227

**Figure 3.** Quartz microstructures in the weakly-undeformed granodiorite (a-b) and in the micro-damage zone of the veins (c-h). BSE images (left column) and their corresponding CL images (right column) with their distance to the vein boundary. Samples 19-37 and 19-38. Mineral abbreviations: *Ab* = albite, *Kfs* = K-feldspar, *Pl* = plagioclase, *Qz* = quartz. (a) Quartz grains outside the micro-damage zone. (b) Undeformed quartz grains show a homogeneous, bright CL signal. (c, e, g) Quartz grains appear almost undeformed in BSE images. (d, f, h) Deformed magmatic quartz shows bright to medium, CL grey-shaded domains, which are pervasively cut by interlaced darker deformation lamellae (DL). These deformation features are cut by CL-dark quartz-filled veinlets. (g-h) Quartz grain close to the vein boundary in the footwall side. In the CL image in (h), the quartz grain appears strongly brecciated (almost pulverized) and is healed by CL-dark quartz.

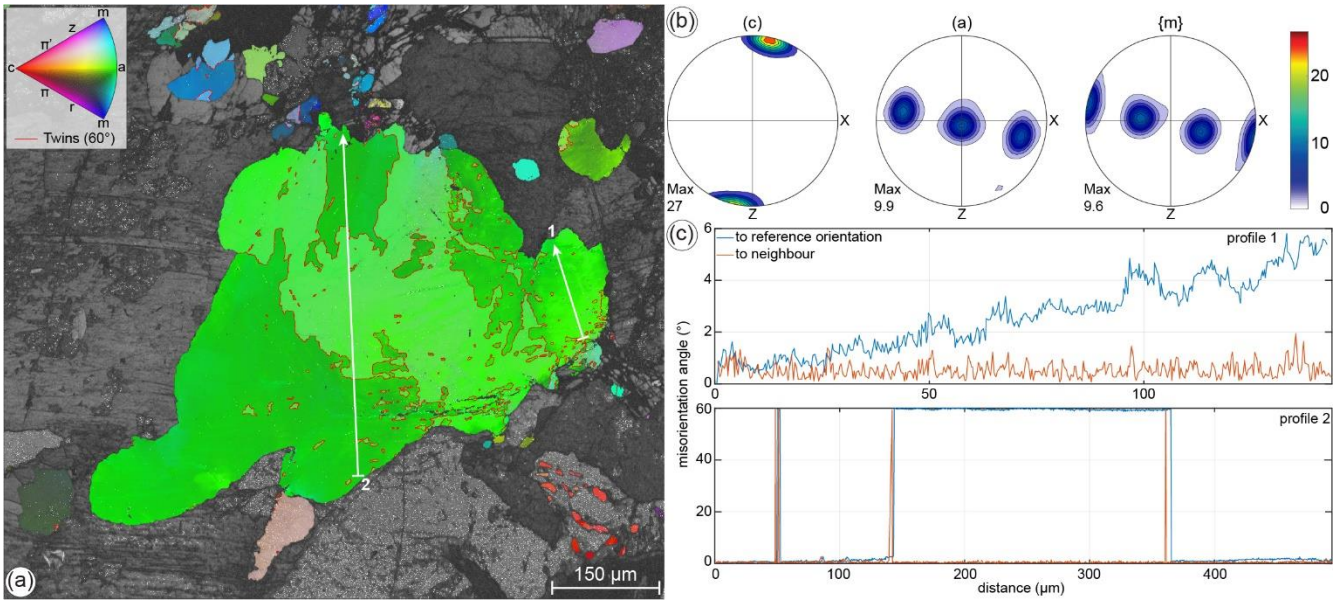


**Figure 4.** EBSD analysis of a deformed magmatic quartz in the micro-damage zone. (a) Inverse Pole Figure (IPF) map, color coded according to IPF legend. The analyzed large magmatic quartz grain is the same shown in Figure 3c-d. The IPF map is overlaid to the orientation contrast image. White lines mark the profiles plotted in (c). (b) Contoured pole figures. (c) Misorientation profiles.

### *4.2. Epidote-rich sheared veins*

The epidote-rich sheared veins have a heterogeneous microstructure (Figures 2e-f, 5-6). Sample 19-48, which includes both sides of the wall-rock surrounding the vein, consists of both undeformed and

cataclastic vein domains (Figures 2c, 2f, 6a). The undeformed domains consist of idiomorphic, zoned epidote (Al-rich; light: Fe-rich; Table S1 in the supporting information) ± prehnite (dark: Al-rich; light: Fe-rich; Table S1 in the supporting information), interstitial chlorite ± quartz ± K-feldspar, and wall-rock fragments (Figures 2c, 5a-b). Undeformed domains are generally present at the outer part of the vein, while the cataclastic domain is at the core (Figures 2c, 6a). The core of the vein consists of a porous fine-grained (< 20 μm in size) matrix of epidote including fragments of earlier vein fillings and of the wall-rock (Figure 2c).

In samples 19-37, 19-38, and 19-46, which only include one side of the footwall wall-rock, the sheared veins consist of layered (proto)cataclasites to ultracataclasites in sharp contact with the topping undeformed vein (Figures 2e-f, 5a, 6b). Close to the wall-rock, the (proto)cataclasites consist of a fine-grained (< 20 μm in size) matrix of zoned epidote ± prehnite with interstitial chlorite (Figure 5c-d), including fragments (up to cm in size) of earlier prehnite-epidote veins and wall-rock (Figure 5a, 5c-d), and some are foliated (Figure 5e). The ultracataclasites consist of a highly porous, fine-grained (≤ 500 nm in size) matrix of epidote and prehnite, with interstitial chlorite, and fragments (up to 100 μm in size) of idiomorphic epidote and prehnite crystals and wall-rock (Figure 5d, 5f-g). Above the lineated slickensides, multiple vein generations are present (Figure 2f, 5a, 5d, 5f). Some veins consist of zoned prehnite crystals elongated orthogonal to the vein boundaries (Figure 5f). Other veins consist of zoned epidote-prehnite crystals, which present localized (ultra)cataclasite layers at the vein boundaries, marking further lineated slickensides (Figures 2f, 5a, 5d).

Fragments of magmatic quartz within the veins appear brecciated under CL (Figure 5h). Micro-fractures are sealed by CL-dark quartz, which rims the brecciated magmatic quartz fragment (Figure 5h). This darker rim shows a faint oscillatory zoning in the external part (Figure 5h). Magmatic quartz included in large (mm in size) wall-rock fragments shows the same deformation features (i.e.,

271 deformation lamellae cut by epitaxial quartz-filled veinlets, Figure 5i-j) as observed in the micro-damage
272 zone (Figure 3).

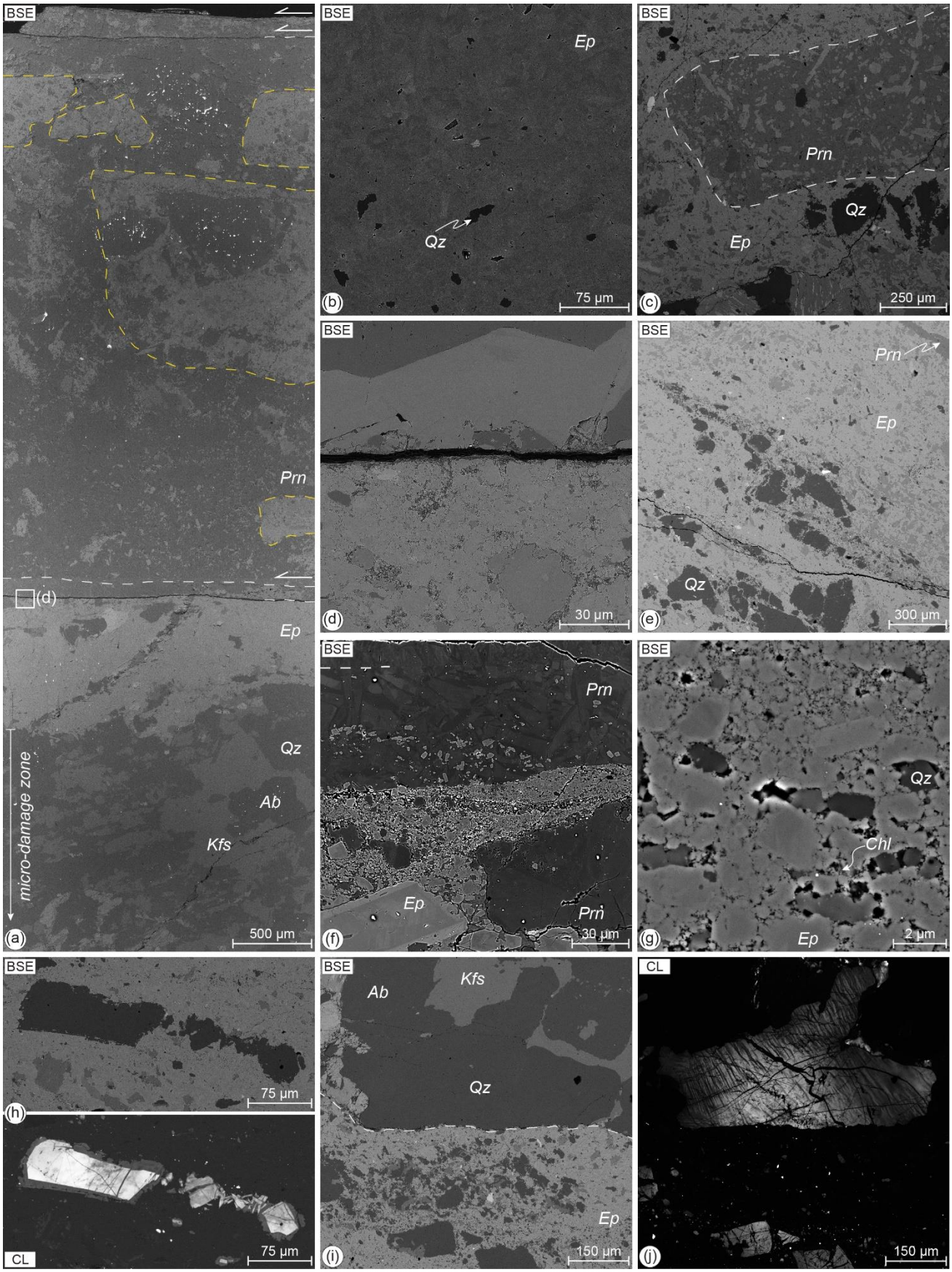
BSE
Prn
(d)
Ep
Qz
Ab
Kfs
micro-damage zone
500 µm
(a)
BSE
Ep
Qz
75 µm
(b)
BSE
Prn
Qz
Ep
250 µm
(c)
BSE
30 µm
(d)
BSE
Prn
Ep
Qz
300 µm
(e)
BSE
Prn
Ep
Prn
30 µm
(f)
BSE
Qz
Chl
Ep
2 µm
(g)
BSE
75 µm
(h)
CL
75 µm
BSE
Ab
Kfs
Qz
Ep
150 µm
(i)
CL
150 µm
(j)

**Figure 5.** Microstructures of the epidote-rich sheared veins (samples 19-37, 19-38, 19-46 and 19-48). Mineral abbreviations: *Ab* = albite, *Chl* = chlorite, *Ep* = epidote, *Kfs* = K-feldspar, *Prn* = prehnite, *Qz* = quartz. (a) Overview of an epidote-prehnite sheared vein and associated footwall block. The sheared vein recorded multiple extensional-to-hybrid veining and along vein-boundary cataclasis. The largest vein includes mm-large fragments of earlier veins (dashed yellow lines) within the cataclastic domain. Dashed white lines indicate the top of each vein boundary. The white box indicates the detail shown in (d). (b) Vein filling consisting of idiomorphic zoned epidote. (c) Angular fragment of an early prehnite-epidote vein (dashed white line) included in epidote-rich vein protocataclasite. (d) Cataclasite with epidote grains overprinted by an extensional vein with epidote-prehnite crystals. (e) Foliated cataclasite. The sigmoidal clast consists of wall-rock fragments with elongated tails of finer fragments and epidote grains. (f) Ultracataclasite, defining the slip zone of a discrete polished surface, includes angular fragments of zoned epidote (light grey) and prehnite (dark grey). Multiple events of extensional-to-hybrid veining reactivate the sheared vein. The latter vein is sealed by elongated prehnite crystals and reactivating a hybrid extensional-shear one. Note the fibrous prehnite crystals above the white dashed line. (g) Matrix of ultracataclasite consisting of epidote nanoparticles ($\leq$ 500 μm in size). Fragmented idiomorphic crystals of epidote and prehnite are included in the matrix. The ultrafine epidote grains have triple junctions and pores ($<<$ 1 μm in size), locally filled with chlorite. (h) Quartz fragments within an epidote cataclasite. The quartz fragments are brecciated and rimmed by CL-darker quartz. (i-j) Quartz grains in wall-rock fragments (the larger is marked by the dashed white line) show the same deformation features observed in the micro-damage zone of the veins, shown in Figure 3.

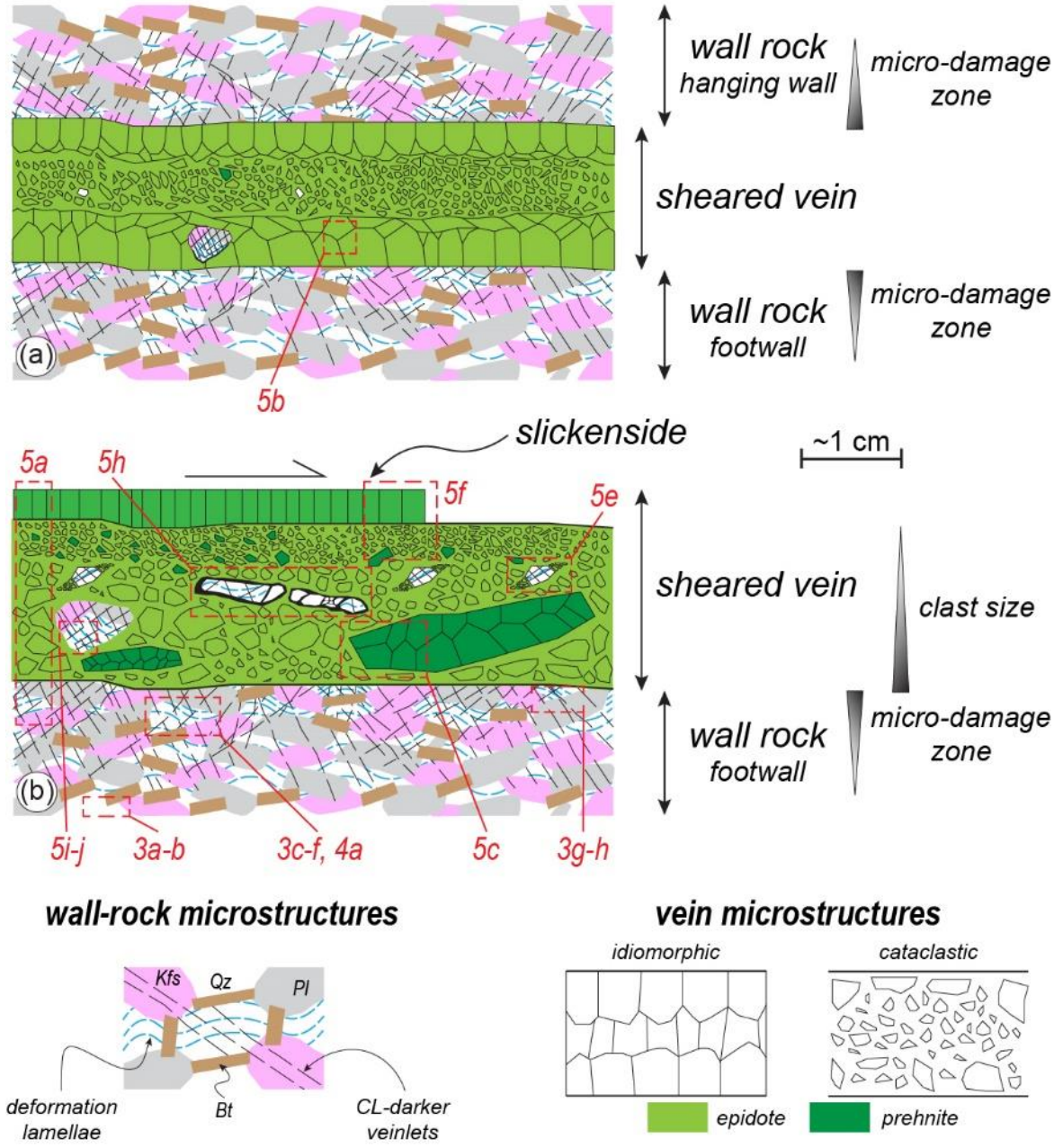


**Figure 6.** Schematic illustration summarizing the different microstructures observed in the epidote-rich sheared veins and associated wall-rock. (a) Sheared veins with both footwall and hanging wall blocks preserved. (b) Sheared veins with only the footwall block preserved.

## 5. Discussion

The epidote-rich fault-vein networks of the BFZ formed at temperatures ≤ 300 °C (Herrera et al., 2005; Masoch et al., 2022), i.e. at conditions close to the brittle-ductile transition for quartz-rich crustal

303 rocks and corresponding to the base of the seismogenic upper crust (Scholz, 2019). Ancient (125-118
304 Ma) seismicity along the BFZ is attested by pseudotachylytes, produced in a fluid-rich environment
305 (Gomila et al., 2021) along the main segments of the fault system (Masoch et al., 2022, 2021). The
306 epidote-rich fault-vein networks represent a subsidiary linkage set of structures that accommodated slip
307 deficit along, and/or slip transfer between, the main seismogenic segments, during fault system growth
308 (Cembrano et al., 2005; Herrera et al., 2005; Masoch et al., 2022, 2021).

309 The SEM images document a polyphase deformation history associated with vein array
310 formation, including (i) an initial stage (well-preserved in the wall-rocks nearby the epidote-rich veins,
311 i.e., micro-damage zone) of fracture propagation with local fluid redistribution along micro-cracks, and
312 (ii) following pulses of hydrothermal fluid infiltration, with of epidote ± prehnite, alternating with vein-
313 parallel cataclastic shearing, which shaped the mature architecture of the fault-fracture system. Below,
314 we discuss the microstructural observations and propose a conceptual model for the nucleation (section
315 5.1) and development (section 5.2) of a highly interconnected fault-fracture network in a seismically-
316 active hydrothermal system (Figure 7), distinguishing two deformation environments (*rock-buffered* vs.
317 *fluid-buffered*) based on the mineralogy of vein fillings. Lastly, we compare our findings with
318 observations of currently active systems (section 5.3).

319

320 *5.1. Wall-rock damage and local fluid redistribution during dynamic crack propagation*

321 Quartz deformation lamellae and quartz-filled veinlets in the micro-damage zone (Figures 3c-h,
322 4) of the epidote-rich fault-veins formed at an early stage of development of the hydrothermal fault-vein
323 system (Figure 7a), as attested by the presence of these microstructures within clasts inside the veins
324 (Figure 5e-g). Quartz deformation lamellae have been reported in shock-impact rocks (e.g., Carter, 1965)
325 and in exhumed middle-crustal shear zones from the Sesia-Lanzo Zone (Western Alps), associated with
326 other high-stress deformation microstructures (e.g., twinning of jadeite, shattering of garnet), as evidence

of upper-crustal seismic ruptures that transiently propagated in the underlying ductile crust (Trepmann & Stöckhert, 2003). Deformation lamellae were produced experimentally in natural quartz deformed under high stresses and relatively low temperatures (400 °C) (Trepmann & Stöckhert, 2013). Similarly, they develop in metals deformed at high-strain rates and low temperatures (Drury, 1993).

During an earthquake rupture propagation, a dynamic transient high-stress field is produced in the immediate surrounding of the rupture tip and leads to instantaneous rock failure and pulverization (Faulkner et al., 2011; Okubo et al., 2019; Reches & Dewers, 2005; Vermilye & Scholz, 1998) as recorded in the wall-rock of several exhumed pseudotachylyte-bearing faults (e.g., Di Toro et al., 2005; Mancktelow et al., 2022; Petley-Ragan et al., 2019). In contrast to seismic ruptures propagating at velocities of $1\text{-}4\times10^{3}$ m/s, micro-cracks may also propagate at extremely low velocities (sub-seismic: $10^{-9}$-$10^{-4}$ m/s) by sub-critical crack growth driven by stress corrosion (Atkinson & Meredith, 1987). Sub-critical crack propagation is particularly efficient in silicate-built rocks in the presence of pressurized water, which maintains crack connectivity, and at high fluid temperatures ($T \geq 200°C$), therefore at the ambient conditions during formation of the fault-vein networks described in this study. However, sub-critical crack propagation cannot explain the high-stress perturbations recorded by the quartz deformation lamellae in the wall-rock surrounding the epidote-rich fault-veins (Trepmann & Stöckhert, 2013) (Figures 3c-h, 4). Thus, in the relatively small-displacement (< 1.5 m) and up to 10s-m-long faults and hybrid fractures of the epidote-rich fault-vein networks, we interpret the occurrence of deformation lamellae in the wall-rock quartz to reflect the high-stress field associated with rupture tip propagation at seismic speeds during initial fracturing (Figure 7a). Blenkinsop & Drury (1988) proposed a similar interpretation for the formation of this low-temperature intra-crystalline deformation microstructure found in the damage zone of the Bayas Fault hosted in quartzites (Cantabrian Zone, Variscan Orogen, Spain).

Quartz-filled veinlets sharply crosscutting the quartz deformation lamellae (Figure 3d, 3f) within the micro-damage zone of the epidote-rich veins (Figures 2e-f, 3-4) increase in spatial density towards the vein boundary (Figure 3), are mostly oriented at high angle with respect to the vein boundary (Figure 3f, 3h), and are healed by the minerals (quartz, K-feldspar and albite) of the crosscut wall-rock (Figures 3c-h, 4). Moreover, at the vein boundary in the footwall blocks, the deformed magmatic quartz is strongly brecciated (Figure 3g-h), resembling *in-situ* shattered or pulverized fault rocks found in exhumed upper to mid-lower crustal seismic fault zones (e.g., Fondriest et al., 2015; Johnson et al., 2021; Mancktelow et al., 2022; Mitchell et al., 2011; Ostermeijer et al., 2022). We therefore infer that the quartz-healed veinlets also resulted from wall-rock damage associated with the dynamic stress field during earthquake rupture tip propagation. Micro-fracturing and rapid healing of seismic faults has been documented in pseudotachylyte-bearing faults hosted in quartzo-feldspathic rocks and referred to the initial stage of seismic rupture propagation (Bestmann et al., 2016, 2012; Mancktelow et al., 2022). Williams & Fagereng (2022) reviewed the role of quartz precipitation in healing seismic faults during the seismic cycle at different environmental conditions and by different mechanisms (e.g., fluid advection, fluid depressurization, dissolution-precipitation creep, frictional heating). The authors observed that, at crustal conditions similar at which the epidote-rich fault-vein networks formed (i.e., temperature $\leq$ 300 °C and 3-7 km depth), micrometer-thick veins can be completely healed by quartz in a timeframe spanning from days to hundreds of years, depending on the mechanisms involved in quartz precipitation. The quartz-filled veinlets are hundreds of µm in length (Figure 3d, 3f. 3h) and up to 15 µm in thickness (Figure 3f) with most veinlets ~2-3-µm-thick (Figure 3d, 3f, 3h). The co-seismic opening of these micro-cracks induced a sudden decrease of pore-fluid pressure ranging from near-lithostatic to sub-MPa levels (e.g., Brantut, 2020; Cox, 2016; Sibson, 1992a, 1992b) that likely resulted in quartz (super)saturation, and eventually into local fluid vaporization (Amagai et al., 2019; Williams, 2019), and in rapid precipitation of amorphous silica (Amagai et al., 2019). Assuming the healing rates estimated by Williams & Fagereng

(2022) (see their Figure 8 and their discussion), the quartz-filled veinlets could have reasonably healed in a timeframe as long as tens of years (considering the largest veinlets), during the co- to post-seismic phase. Moreover, the veinlet filling is controlled in composition by the crosscut wall-rock minerals (quartz ± K-feldspar ± albite; Figure 3c-h), discarding any extensive fluid advection from external reservoirs (Williams & Fagereng, 2022). This observation also indicates that the co-to-post-seismic micro-fracture formation and healing occurred in a *rock-buffered* system, where percolation of external hydrothermal fluids or fluid redistribution was still minor, owing to the still immature stage of development of a fully interconnected network of permeable fractures and more conspicuous fluid circulation (Figure 7a). In summary, the microstructures preserved in the deformed magmatic quartz in the proximity of epidote-rich sheared veins resulted from dynamic propagation of seismic ruptures and co- to post-seismic healing of a newly-produced micro-fracture network. Both low-temperature crystal-plasticity (deformation lamellae in quartz) and micro-fracturing accommodated the high-stress conditions around a propagating seismic rupture (Figure 7a).

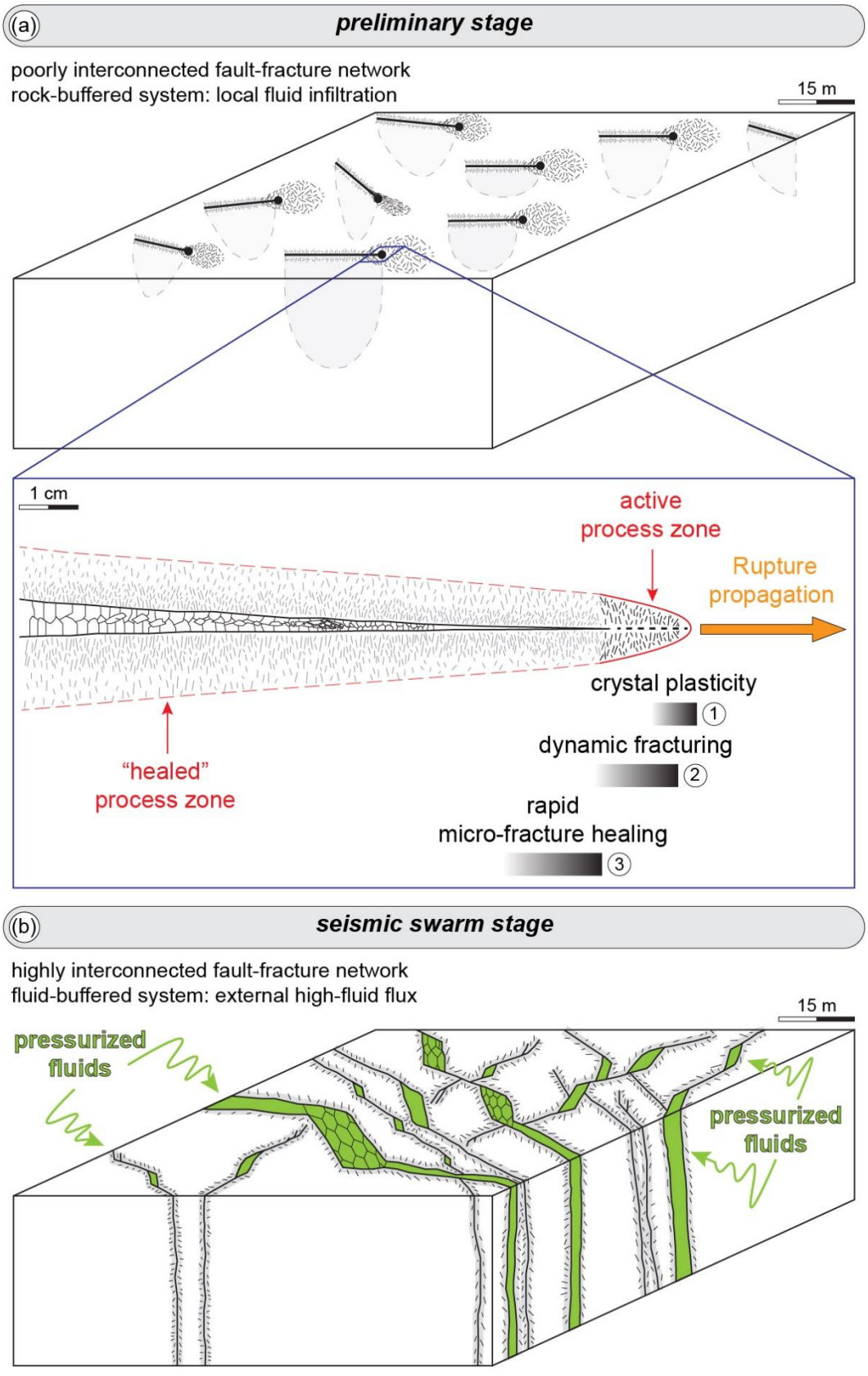
(a)
preliminary stage
poorly interconnected fault-fracture network
rock-buffered system: local fluid infiltration
15 m
1 cm
active
process zone
Rupture
propagation
crystal plasticity
1
dynamic fracturing
2
rapid
micro-fracture healing
3
"healed"
process zone
(b)
seismic swarm stage
highly interconnected fault-fracture network
fluid-buffered system: external high-fluid flux
15 m
pressurized
fluids
pressurized
fluids

388

**Figure 7.** Conceptual model summarizing the development of the seismically-active hydrothermal system recorded in the studied epidote-rich fault-vein networks. (a) Stage 1: initial stages of dynamic propagation of small seismic ruptures. The fault-fracture network is poorly interconnected, and, in turn, fluid circulation is relatively low and at cm-scale (*rock-buffered system*). The blue box marks the zoom at the crack tip and shows the sequences of deformation processes that recorded the initial stages, well preserved in the wall-rocks, of seismic rupture propagation. (b) Stage 2: distributed swarm-like seismicity (*fluid-buffered system*). Highly-interconnected fault-fracture networks allow the ingression of overpressured fluids leading to swarm-like earthquake sequences, well recorded in the sheared veins. The cyclic deformation sequence is driven by fluid pressure fluctuations as illustrated in Figure 8.

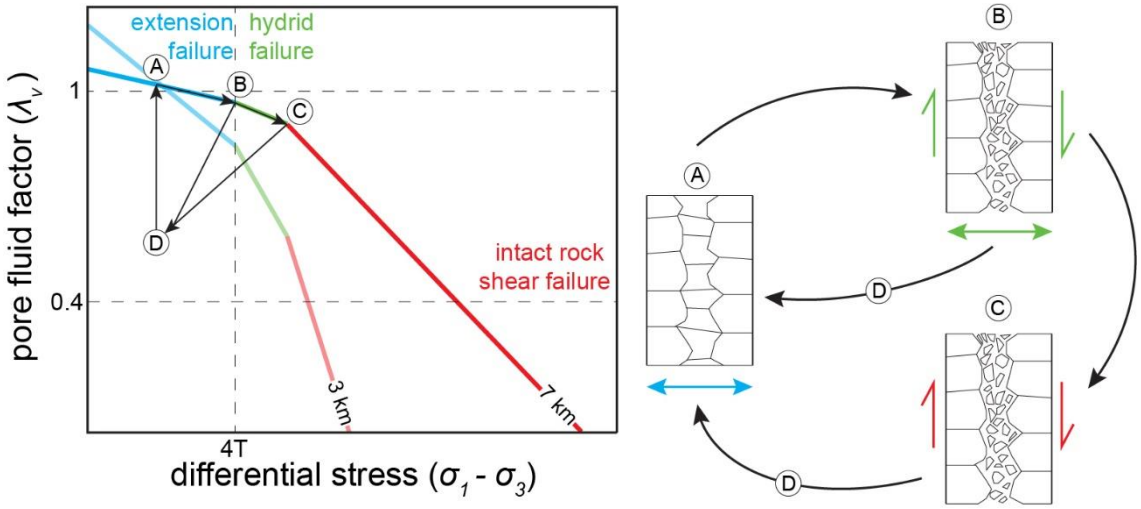


**Figure 8.** λ – Δσ diagram (left) and cartoon (right) illustrating the deformation cycle governing seismicity during the swarm stage. Failure curves represented for the minimum and maximum formation depths of the epidote-rich fault-vein network. The schematic λ – Δσ diagram illustrates the fluid pressure vs. tectonic stress paths recorded by the sheared veins, which show cyclic fluid-driven extensional-to-hybrid veining and shearing. The evolution of fluid pressure and stress states controls the temporal evolution and deformation path of swarm sequence till fluid depletion.

### *5.2. Pore pressure oscillations in a highly connected hydrothermal (fluid-buffered) fault-fracture network*

The epidote-rich veining and shearing postdate the initial short-term co- to post-seismic deformation recorded in the deformed wall-rock magmatic quartz, as discussed in the previous section.

411 The initial fracturing and associated wall-rock damage was precursory to development of a more robust
412 external fluid ingression within the initially low-permeability crystalline rocks (Figure 7). Robust fluid
413 ingression was accompanied by a switch from the initially fluid-poor *rock-buffered* system to a *fluid-*
414 *buffered* one (Figure 7b). In hydrothermal systems, rock failure is governed by fault-valve behavior
415 (Sibson, 1989, 1992a, 1992b), associated with transient fluctuations in pore fluid pressure.

416 The epidote-rich fault-vein networks show cyclic and mutually overprinting events of extensional
417 veining and shearing (Figures 2e-f, 5a-d). Cataclasites include fragments of earlier veins (Figures 2b-c,
418 2e-f, 5a-d), indicating that extensional veining preceded either hybrid extensional-shear fracturing
419 (Figures 2b, 5c) or shearing (Figure 2a). Cataclasites are overprinted by extensional(-shear) veins, which
420 show cataclastic shearing along vein boundaries (Figures 2f, 5a, 5d, 5f). Some cataclasites are foliated
421 (Figure 5e) suggesting that slip likely occurred by aseismic fault creep (e.g., Chester & Chester, 1998;
422 Rutter et al., 1986). On the other hand, most cataclasites display suspended clasts of wall-rocks and
423 earlier veins (Figures 2e, 5a, 5c, 5h-j) similar to the microstructures observed in fluidized cataclasites
424 and breccias, which have been interpreted as markers of co-seismic slip (e.g., Cox, 2016; Fondriest et
425 al., 2012; Masoch et al., 2019; Smith et al., 2008).

426 The overprinting between extensional veining and shearing can be interpreted with the use of $\lambda$
427 $- \Delta\sigma$ failure mode diagrams (Cox, 2010), where $\lambda$ is the pore fluid factor ($\lambda = \frac{p}{\sigma_v}$ ; where $p$ and $\sigma_v$ is the
428 pore fluid pressure and the vertical stress, respectively) and $\Delta\sigma$ is the differential stress ($\Delta\sigma = \sigma_1 - \sigma_3$;
429 where $\sigma_1$ and $\sigma_3$ are the maximum and minimum principal compressive stresses, respectively). At low
430 differential stresses ($\Delta\sigma < 4T$ ; where $T$ is the tensile strength of the material) and larger rate of increase
431 in pore fluid pressure respect to the increase in tectonic loading, hydraulic fracturing (and extensional
432 veining) occurs before shear failure (Murrel-Griffith failure criteria; Price & Cosgrove, 1990) (step A,
433 Figure 8). Opening of extensional fractures prevents further increase in fluid pressure and pressurizes the
434 fracture network. The progressive increase in tectonic-related differential stress leads to hybrid

435 extensional-shear failure (step B, Figure 8) to shear failure (step C, Figure 8), causing stress drop and
436 fault depressurization (step D, Figure 8). The progressive increase in tectonic-related differential stress
437 could be achieved because the NE-, SW- and NW-dipping small-displacement epidote-rich vein arrays
438 are (near-)optimally oriented with respect to the tectonic stress field (i.e., nearly subvertical-oriented
439 compression direction; Cembrano et al., 2005; Veloso et al., 2015). The described deformation cycle can
440 repeatedly occur if the system is dominated by increase rate of fluid pressure larger than increase rate of
441 tectonic loading (Cox, 2016; Phillips, 1972). However, we cannot rule out that part of the cyclic
442 deformation history recorded by the epidote-rich veins is the result of deformation events unrelated to
443 the coupled evolution of fluid pressure and tectonic differential stress.
444
445 *5.3. Comparison with natural fluid-driven earthquake swarms*
446 Earthquake swarms are characterized by a spatiotemporal clustering of large number of small
447 magnitude events, without a clear triggering mainshock (Mogi, 1963). Such a behavior requires external
448 mechanisms driving seimsicity, among which fluid diffusion and aseismic slip are the preferred ones
449 (e.g., De Barros et al., 2020; Lohman & McGuire, 2007; Vidale & Shearer, 2006). Recent studies
450 revealed that both processes can coexists with fluid diffusion favoring the occurrence of aseismic slip,
451 which triggers seismicity by stress transfer ahead of the slip front (e.g., Danré et al., 2022; Guglielmi et
452 al., 2015). The occurrence of swarms is also controlled by the complexity of fault systems, such as fault
453 linkages, step-overs, or hydrated fracture zones (e.g., Essing & Poli, 2022; Legrand et al., 2011; Poli et
454 al., 2017; Ross et al., 2020, 2017; Shelly et al., 2022). For instance, thanks to high-precision earthquake
455 relocation, Shelly et al. (2022) documented that two conjugate sets of strike-slip faults well-oriented with
456 respect to the far-field stress were activated during the swarm-like 2020 Maacama sequence. Most
457 earthquakes had moment magnitude $M_W < 1$ and localized in overstepping segments of the Maacana
458 Fault (Northern California). Moreover, swarm-like sequences produce both non-double-couple (i.e.,

459 isotropic) and double-couple events in the same period of time, resulting from co-seismic fault opening
460 (dilation) and shearing, respectively (e.g., Legrand et al., 2011; Shelly et al., 2013).

461 Our geological observations (Figures 1-2, 5) show several analogies with the characteristics of
462 earthquake swarms. At Stage 1, we infer the early development of a fault-fracture mesh within a low-
463 permeability intact rock volume, producing the pathways for the ingression of external pressurized
464 hydrothermal fluids sustaining the swarmogenic activity of Stage 2 (Figures 7b-8). The microstructures
465 found in the micro-damage zones of the veins and hybrid fractures (i.e., quartz deformation lamellae and
466 quartz-filled veinlets; Figures 3-4) are consistent with rupture propagation of small-in-magnitude
467 earthquakes, possibly also accompanied by quasi-static crack growth (Stage 1, Figure 7a). The fault-
468 fracture network progressively became hydraulically more connected during Stage 2 (Figure 7b). Cyclic
469 fluid pressure fluctuations drove widespread epidote precipitation and development of the epidote-rich
470 hybrid fracture and vein system (Figures 7b-8). We associate this stage with the activation of a
471 swarmogenic system (Figure 7b) as suggested by the following analogies between our geological
472 observations and earthquake swarms:

473 1. *Fault geometric complexity*: the small-displacement (< 1.5 m) veins are located at geometric
474 complexities, such as fault linkages and intersections (Figure 1b), within the crustal Coloso
475 Duplex (Cembrano et al., 2005; Masoch et al., 2022) (Figure 1a). The fault-vein system is
476 arranged into sets (i.e., NW-, NE- and SW-dipping fault-veins; Figure 1c) (near-)optimally
477 oriented with respect to the local-stress field (i.e., subvertical-oriented $\sigma_1$; Cembrano et al.,
478 2005; Veloso et al., 2015). Many works have shown that fault geometric complexities are the
479 *loci* for the development of earthquake swarms (e.g., Legrand et al., 2011; Ross et al., 2020,
480 2017), commonly activing fault-fracture networks well-oriented with the stress field (Shelly
481 et al., 2022). Moreover, this structural arrangement forms a honey mesh-like fault network at

482 the scale up to 100s of meter (Figure 1b), which is the fault-fracture geometry commonly
483 inferred to be activated during swarms (Hill, 1977; Sibson, 1996).
484 2. *Fluid diffusion within the fault system*: faulting was driven by the ingression of pressurized
485 fluids within the fault system (section 5.2) and the veins recorded cyclic extensional-to-hybrid
486 veining and shearing (Figures 2b-f, 5a-g), which might be interpreted as the source of non-
487 double-couple (crack opening) and double-couple (shear fracture) processes occurring in
488 swarm-like sequences (e.g., Legrand et al., 2011; Shelly et al., 2013). Bursts of short-lasting
489 (tens to thousands of seconds) fluid pressure variations trigger repeated small earthquakes
490 along active fault systems (Collettini, 2002; Essing & Poli, 2022; Piana Agostinetti et al.,
491 2017). Similarly, such a repeated condition of fluid (over-)pressurization in short timespans
492 drives the deformation cycle (i.e., crack opening followed by along vein-boundary slip)
493 recorded in the veins (Figure 5a, 5c-g) and described by the diagram in Figure 8.
494 3. *Coexistence of both aseismic and seismic slip*: the sheared veins accommodated either
495 aseismic fault slip, as attested by foliated cataclastic horizons (Figure 5e), and possible
496 seismic fault slip, as documented by the occurrence of suspended clasts within cataclasites
497 (Figures 2e, 5a, 5c, 5h-j), mutually overprinting crack opening (i.e., extensional veins) (Figure
498 5a, 5f). The occurrence of both slip behaviors, coupled with fluid pressure diffusion, has been
499 recently observed in the both natural swarm-like sequences (Danré, De Barros, Cappa, et al.,
500 2022) and fluid-injection experiments (Guglielmi et al., 2015).
501 4. *Small scale length*: the veins extend for tens of meters in length (Figure 1b) and have a
502 thickness up to 2-3 cm (Figure 2b-c), resulted from multiple events of crack opening and
503 fracture shearing (Figures 2b-c, 2e-f, 5a, 5c-d, 5f-g). Considering that each crack opening
504 episode results in dilatant slip ranging from tens to hundreds of μm (Figures 2f, 5a, 5f), these

505 are equivalent to micro-seismic events with $-2 < M_W < 0$ (Wells & Coppersmith, 1994), which
506 is the magnitude range typical of earthquake swarms (Mogi, 1963).
507
508 **6. Conclusions**
509 The extensive epidote-rich fault-vein networks of the damage zone of Bolfin Fault Zone and of
510 the Coloso Duplex, at larger scale, are exceptionally well-exposed over tens of square kilometers in the
511 Atacama Desert (Northern Chile) (Figure 1). The fault-vein networks are spatially distributed around
512 major transtensional pseudotachylyte-bearing faults of the duplex, and consist of fault-veins with lineated
513 slickenside, extensional veins and dilatant breccias (Figure 2). Based on microstructural analysis, we
514 document that the wall-rocks in proximity to small-displacement (< 1.5 m) fault-veins initially
515 experienced dynamic high stresses related to the propagation of small seismic ruptures in a poorly
516 connected fault-fracture system with limited fluid infiltration (Figures 3-4, 7a). Instead, the epidote-rich
517 fault-veins recorded cyclic crack opening and either seismic or aseismic shearing dominated by fluid
518 pressure fluctuations in a mature and highly interconnected fault-fracture system (Figures 5-6, 7b, 8). As
519 a consequence, the epidote-rich fault-vein networks of the Bolfin Fault Zone and, at larger scale, of the
520 Coloso Duplex represent the mature architecture of a fault-fracture system in a high-fluid flux
521 hydrothermal setting. Thus, the Coloso Duplex is interpreted as a fossil example of an upper-crustal
522 seismogenic hydrothermal system, which generated fluid-driven earthquake swarms.
523
524
525 **Acknowledgements**
526 This research was funded by ERC CoG project NOFEAR 614705 to GDT. SM acknowledges Fondazione
527 CARIPARO (PhD scholarship), Fondazione Ing. Aldo Gini and the School of Science of Università degli
528 Studi di Padova (staying in Chile). GP and GDT acknowledge funding from PRIN 2020WPMFE9. MF

529 received funding from the EU Horizon 2020 MSCA-IF DAMAGE (No. 839880), from
530 NextGenerationEU (REACT project) and from the 2021 STARS Grants@Unipd programme (STIFF
531 project). RG have received funding from the European Union's Horizon 2020 research and innovation
532 program under the Marie Skłodowska-Curie grant agreement No 896346 (FRICTION). JC acknowledges
533 support by Fondecyt grant #1210591, on fluid transport through vein networks and at fault intersections
534 in the crust. We thank Leonardo Tauro and Silvia Cattò (thin sections), Nicola Michelon (scans of thin
535 sections), Stefano Castelli (scans of polished samples), and Jacopo Nava (technical assistance using
536 electron microscopy). SM thanks Giovanni Toffol for help with MTEX. The EBSD data are available at
537 the repository with the following link: https://researchdata.cab.unipd.it/id/eprint/898. We acknowledge
538 Stephen Cox, Christie Rowe, Catriona Menzies and Randy Williams for commenting an early version of
539 this manuscript.

540

541 **CRediT author statement**

542 **Simone Masoch**: Conceptualization, Formal analysis, Investigation, Writing – Original Draft,
543 Visualization, Funding acquisition. **Giorgio Pennacchioni**: Conceptualization, Investigation, Writing –
544 Review & Editing, Supervision. **Michele Fondriest**: Conceptualization, Writing – Review & Editing.
545 **Rodrigo Gomila**: Writing – Review & Editing. **Piero Poli**: Conceptualization, Writing – Review &
546 Editing. **José Cembrano**: Writing – Review & Editing, Supervision. **Giulio Di Toro**: Conceptualization,
547 Writing – Review & Editing, Supervision, Project administration, Funding acquisition.

548

549 **References**

550 Amagai, T., Okamoto, A., Niibe, T., Hirano, N., Motomiya, K., & Tsuchiya, N. (2019). Silica
551 nanoparticles produced by explosive flash vaporization during earthquakes. *Scientific Reports*, *9*(1),
552 9738. https://doi.org/10.1038/s41598-019-46320-7

Arabasz, W. J. J. (1971). *Geological and geophysical studies of the Atacama fault zone in northern Chile*. PhD thesis, California Institute of Technology, Pasadena.

Atkinson, B. K., & Meredith, P. G. (1987). The theory of subcritical crack growth with application to mineral and rocks. In *Fracture Mechanics of Rocks* (pp. 111–166). Academic Press.

Baques, M., De Barros, L., Godano, M., Duverger, C., & Jomard, H. (2023). Swarms and mainshock–aftershocks sequences are both triggered by fluids in the Ubaye Region (Western Alps). *Geophysical Journal International*, *235*(1), 920–941. https://doi.org/10.1093/gji/ggad280

Behr, W. M., & Platt, J. P. (2014). Brittle faults are weak, yet the ductile middle crust is strong: Implications for lithospheric mechanics. *Geophysical Research Letters*, *41*(22), 8067–8075. https://doi.org/10.1002/2014GL061349

Bestmann, M., Pennacchioni, G., Mostefaoui, S., Göken, M., & de Wall, H. (2016). Instantaneous healing of micro-fractures during coseismic slip: Evidence from microstructure and Ti in quartz geochemistry within an exhumed pseudotachylyte-bearing fault in tonalite. *Lithos*, *254–255*, 84–93. https://doi.org/10.1016/j.lithos.2016.03.011

Bestmann, M., Pennacchioni, G., Nielsen, S., Göken, M., & de Wall, H. (2012). Deformation and ultrafine dynamic recrystallization of quartz in pseudotachylyte-bearing brittle faults: A matter of a few seconds. *Journal of Structural Geology*, *38*, 21–38. https://doi.org/10.1016/j.jsg.2011.10.001

Blenkinsop, T. G., & Drury, M. R. (1988). Stress estimates and fault history from quartz microstructures. *Journal of Structural Geology*, *10*(7), 673–684. https://doi.org/10.1016/0191-8141(88)90075-2

Boullier, A.-M., & Robert, F. (1992). Palaeoseismic events recorded in Archaean gold-quartz vein networks, Val d'Or, Abitibi, Quebec, Canada. *Journal of Structural Geology*, *14*(2), 161–179. https://doi.org/10.1016/0191-8141(92)90054-Z

Brantut, N. (2020). Dilatancy-induced fluid pressure drop during dynamic rupture: Direct experimental evidence and consequences for earthquake dynamics. *Earth and Planetary Science Letters*, *538*,

116179. https://doi.org/10.1016/j.epsl.2020.116179

Caine, J. S., Evans, J. P., & Forster, C. B. (1996). Fault zone architecture and permeability structure. *Geology*, *24*(11), 1025–1028. https://doi.org/10.1130/0091-7613(1996)024<1025:FZAAPS>2.3.CO;2

Carter, N. (1965). Basal quartz deformation lamellae - A criterion for recognition of impactites. *American Journal of Science*, *263*.

Cembrano, J., González, G., Arancibia, G., Ahumada, I., Olivares, V., & Herrera, V. (2005). Fault zone development and strain partitioning in an extensional strike-slip duplex: A case study from the Mesozoic Atacama fault system, Northern Chile. *Tectonophysics*, *400*(1–4), 105–125. https://doi.org/10.1016/j.tecto.2005.02.012

Cembrano, J., & Lara, L. (2009). The link between volcanism and tectonics in the southern volcanic zone of the Chilean Andes: A review. *Tectonophysics*, *471*(1–2), 96–113. https://doi.org/10.1016/j.tecto.2009.02.038

Cerchiari, A., Remitti, F., Mittempergher, S., Festa, A., Lugli, F., & Cipriani, A. (2020). Cyclical variations of fluid sources and stress state in a shallow megathrust-zone mélange. *Journal of the Geological Society*, *177*(3), 647–659. https://doi.org/10.1144/jgs2019-072

Chester, F. M., & Chester, J. S. (1998). Ultracataclasite structure and friction processes of the Punchbowl fault, San Andreas system, California. *Tectonophysics*, *295*(1–2), 199–221. https://doi.org/10.1016/S0040-1951(98)00121-8

Collettini, C. (2002). Hypothesis for the mechanics and seismic behaviour of low-angle normal faults: The example of the Altotiberina fault northern Apennines. *Annals of Geophysiscs*, *45*(5).

Cox, S. F. (2010). The application of failure mode diagrams for exploring the roles of fluid pressure and stress states in controlling styles of fracture-controlled permeability enhancement in faults and shear zones. *Geofluids*. https://doi.org/10.1111/j.1468-8123.2010.00281.x

601 Cox, S. F. (2016). Injection-Driven Swarm Seismicity and Permeability Enhancement: Implications for
602 the Dynamics of Hydrothermal Ore Systems in High Fluid-Flux, Overpressured Faulting
603 Regimes—An Invited Paper. *Economic Geology*, *111*(3), 559–587.
604 https://doi.org/10.2113/econgeo.111.3.559
605 Cox, S. F. (2020). Chapter 2: The Dynamics of Permeability Enhancement and Fluid Flow in
606 Overpressured, Fracture-Controlled Hydrothermal Systems. In *Applied Structural Geology of Ore-*
607 *forming Hydrothermal Systems* (pp. 25–82). https://doi.org/10.5382/rev.21.02
608 Cox, S. F., & Munroe, S. M. (2016). Breccia formation by particle fluidization in fault zones:
609 Implications for transitory, rupture-controlled fluid flow regimes in hydrothermal systems.
610 *American Journal of Science*, *316*(3), 241–278. https://doi.org/10.2475/03.2016.02
611 Danré, P., De Barros, L., & Cappa, F. (2022). Inferring fluid volume during earthquake swarms using
612 seismic catalogues. *Geophysical Journal International*, *232*(2), 829–841.
613 https://doi.org/10.1093/gji/ggac345
614 Danré, P., De Barros, L., Cappa, F., & Ampuero, J. (2022). Prevalence of Aseismic Slip Linking Fluid
615 Injection to Natural and Anthropogenic Seismic Swarms. *Journal of Geophysical Research: Solid*
616 *Earth*, *127*(12). https://doi.org/10.1029/2022JB025571
617 De Barros, L., Cappa, F., Deschamps, A., & Dublanchet, P. (2020). Imbricated Aseismic Slip and Fluid
618 Diffusion Drive a Seismic Swarm in the Corinth Gulf, Greece. *Geophysical Research Letters*, *47*(9).
619 https://doi.org/10.1029/2020GL087142
620 Dempsey, E. D., Holdsworth, R. E., Imber, J., Bistacchi, A., & Di Toro, G. (2014). A geological
621 explanation for intraplate earthquake clustering complexity: The zeolite-bearing fault/fracture
622 networks in the Adamello Massif (Southern Italian Alps). *Journal of Structural Geology*, *66*, 58–
623 74. https://doi.org/10.1016/j.jsg.2014.04.009
624 Derez, T., Pennock, G., Drury, M., & Sintubin, M. (2015). Low-temperature intracrystalline deformation

microstructures in quartz. *Journal of Structural Geology*, *71*, 3–23. https://doi.org/10.1016/j.jsg.2014.07.015

Di Toro, G., Nielsen, S., & Pennacchioni, G. (2005). Earthquake rupture dynamics frozen in exhumed ancient faults. *Nature*, *436*(7053), 1009–1012. https://doi.org/10.1038/nature03910

Dorbath, L., Cuenot, N., Genter, A., & Frogneux, M. (2009). Seismic response of the fractured and faulted granite of Soultz-sous-Forêts (France) to 5 km deep massive water injections. *Geophysical Journal International*, *177*(2), 653–675. https://doi.org/10.1111/j.1365-246X.2009.04030.x

Drury, M. R. (1993). Deformation lamellae in metals and minerals. In J. N. Boland & J. D. Fitzgerald (Eds.), *Defects and Processes in the Solid State: Geoscience Applications* (pp. 195–212). The McLaren Volume.

Ellsworth, W. L. (2013). Injection-Induced Earthquakes. *Science*, *341*(6142). https://doi.org/10.1126/science.1225942

Enescu, B., Hainzl, S., & Ben-Zion, Y. (2009). Correlations of Seismicity Patterns in Southern California with Surface Heat Flow Data. *Bulletin of the Seismological Society of America*, *99*(6), 3114–3123. https://doi.org/10.1785/0120080038

Essing, D., & Poli, P. (2022). Spatiotemporal Evolution of the Seismicity in the Alto Tiberina Fault System Revealed by a High-Resolution Template Matching Catalog. *Journal of Geophysical Research: Solid Earth*. https://doi.org/https://doi.org/10.1029/2022JB024845

Fairbairn, H. (1941). Deformation lamellae in quartz from the Ajibik Formation, Michigan. *Geological Society of America Bulletin*, *52*, 1265–1278.

Faulkner, D. R., Jackson, C. A. L., Lunn, R. J., Schlische, R. W., Shipton, Z. K., Wibberley, C. A. J., & Withjack, M. O. (2010). A review of recent developments concerning the structure, mechanics and fluid flow properties of fault zones. *Journal of Structural Geology*, *32*(11), 1557–1575. https://doi.org/10.1016/j.jsg.2010.06.009

649 Faulkner, D. R., Mitchell, T. M., Healy, D., & Heap, M. J. (2006). Slip on "weak" faults by the rotation
650 of regional stress in the fracture damage zone. *Nature*, *444*(7121), 922–925.
651 https://doi.org/10.1038/nature05353
652 Faulkner, D. R., Mitchell, T. M., Jensen, E., & Cembrano, J. (2011). Scaling of fault damage zones with
653 displacement and the implications for fault growth processes. *Journal of Geophysical Research:*
654 *Solid Earth*, *116*(5), 1–11. https://doi.org/10.1029/2010JB007788
655 Fischer, T., Horálek, J., Hrubcová, P., Vavryčuk, V., Bräuer, K., & Kämpf, H. (2014). Intra-continental
656 earthquake swarms in West-Bohemia and Vogtland: A review. *Tectonophysics*, *611*, 1–27.
657 https://doi.org/10.1016/j.tecto.2013.11.001
658 Fondriest, M., Aretusini, S., Di Toro, G., & Smith, S. A. F. (2015). Fracturing and rock pulverization
659 along an exhumed seismogenic fault zone in dolostones: The Foiana Fault Zone (Southern Alps,
660 Italy). *Tectonophysics*, *654*, 56–74. https://doi.org/10.1016/j.tecto.2015.04.015
661 Fondriest, M., Smith, S. A. F., Di Toro, G., Zampieri, D., & Mittempergher, S. (2012). Fault zone
662 structure and seismic slip localization in dolostones, an example from the Southern Alps, Italy.
663 *Journal of Structural Geology*, *45*, 52–67. https://doi.org/10.1016/j.jsg.2012.06.014
664 Genna, A., Jébrak, M., Marcoux, E., & Milési, J. P. (1996). Genesis of cockade breccias in the tectonic
665 evolution of the Cirotan epithermal gold system, West Java. *Canadian Journal of Earth Sciences*,
666 *33*(1), 93–102. https://doi.org/10.1139/e96-010
667 Goebel, T. H. W., Hosseini, S. M., Cappa, F., Hauksson, E., Ampuero, J. P., Aminzadeh, F., & Saleeby,
668 J. B. (2016). Wastewater disposal and earthquake swarm activity at the southern end of the Central
669 Valley, California. *Geophysical Research Letters*, *43*(3), 1092–1099.
670 https://doi.org/10.1002/2015GL066948
671 Gomila, R., Fondriest, M., Jensen, E., Spagnuolo, E., Masoch, S., Mitchell, T. M., … Di Toro, G. (2021).
672 Frictional Melting in Hydrothermal Fluid-Rich Faults: Field and Experimental Evidence From the

673 Bolfín Fault Zone (Chile). *Geochemistry, Geophysics, Geosystems*, *22*(7).
674 https://doi.org/10.1029/2021GC009743
675 Guglielmi, Y., Cappa, F., Avouac, J.-P., Henry, P., & Elsworth, D. (2015). Seismicity triggered by fluid
676 injection–induced aseismic slip. *Science*, *348*(6240), 1224–1226.
677 https://doi.org/10.1126/science.aab0476
678 Handy, M. R., Hirt, G., & Hovius, N. (2007). *Tectonic Faults. Agents of Change on a Dynamic Earth*.
679 Cambdrige, Massachusetts. London, Uk.: The MIT Press.
680 Healy, J. H., Rubey, W. W., Griggs, D. T., & Raleigh, C. B. (1968). The Denver Earthquakes. *Science*,
681 *161*(3848), 1301–1310. https://doi.org/10.1126/science.161.3848.1301
682 Herrera, V., Cembrano, J., Olivares, V., Kojima, S., & Arancibia, G. (2005). Precipitación por
683 despresurización y ebullición en vetas hospedadas en un dúplex de rumbo extensional: Evidencias
684 microestructurales y microtermométricas. *Revista Geologica de Chile*, *32*(2), 207–227.
685 Hill, D. P. (1977). A model for earthquake swarms. *Journal of Geophysical Research*, *82*(8), 1347–1352.
686 https://doi.org/10.1029/JB082i008p01347
687 Jensen, E., Cembrano, J., Faulkner, D., Veloso, E., & Arancibia, G. (2011). Development of a self-similar
688 strike-slip duplex system in the Atacama Fault system, Chile. *Journal of Structural Geology*, *33*(11),
689 1611–1626. https://doi.org/10.1016/j.jsg.2011.09.002
690 Johnson, S. E., Song, W. J., Vel, S. S., Song, B. R., & Gerbi, C. C. (2021). Energy Partitioning, Dynamic
691 Fragmentation, and Off-Fault Damage in the Earthquake Source Volume. *Journal of Geophysical*
692 *Research: Solid Earth*, *126*(11). https://doi.org/10.1029/2021JB022616
693 Legrand, D., Barrientos, S., Bataille, K., Cembrano, J., & Pavez, A. (2011). The fluid-driven tectonic
694 swarm of Aysen Fjord, Chile (2007) associated with two earthquakes (Mw=6.1 and Mw=6.2) within
695 the Liquiñe-Ofqui Fault Zone. *Continental Shelf Research*, *31*(3–4), 154–161.
696 https://doi.org/10.1016/j.csr.2010.05.008

Lohman, R. B., & McGuire, J. J. (2007). Earthquake swarms driven by aseismic creep in the Salton Trough, California. *Journal of Geophysical Research: Solid Earth*, *112*(B4). https://doi.org/10.1029/2006JB004596

Lucca, A., Storti, F., Balsamo, F., Clemenzi, L., Fondriest, M., Burgess, R., & Di Toro, G. (2019). From Submarine to Subaerial Out-of-Sequence Thrusting and Gravity-Driven Extensional Faulting: Gran Sasso Massif, Central Apennines, Italy. *Tectonics*, *38*(12), 4155–4184. https://doi.org/10.1029/2019TC005783

Malatesta, C., Crispini, L., Ildefonse, B., Federico, L., Lisker, F., & Läufer, A. (2021). Microstructures of epidote-prehnite bearing damaged granitoids (northern Victoria Land, Antarctica): clues for the interaction between faulting and hydrothermal fluids. *Journal of Structural Geology*, *147*, 104350. https://doi.org/10.1016/j.jsg.2021.104350

Mancktelow, N. S., Camacho, A., & Pennacchioni, G. (2022). Time-Lapse Record of an Earthquake in the Dry Felsic Lower Continental Crust Preserved in a Pseudotachylyte-Bearing Fault. *Journal of Geophysical Research: Solid Earth*, *127*(4). https://doi.org/10.1029/2021JB022878

Masoch, S., Fondriest, M., Gomila, R., Jensen, E., Mitchell, T. M., Cembrano, J., … Di Toro, G. (2022). Along-strike architectural variability of an exhumed crustal-scale seismogenic fault (Bolfin Fault Zone, Atacama Fault System, Chile). *Journal of Structural Geology*, *165*, 104745. https://doi.org/10.1016/j.jsg.2022.104745

Masoch, S., Fondriest, M., Preto, N., Secco, M., & Di Toro, G. (2019). Seismic cycle recorded in cockade-bearing faults (Col de Teghime, Alpine Corsica). *Journal of Structural Geology*, *129*, 103889. https://doi.org/10.1016/j.jsg.2019.103889

Masoch, S., Gomila, R., Fondriest, M., Jensen, E., Mitchell, T., Pennacchioni, G., … Di Toro, G. (2021). Structural Evolution of a Crustal-Scale Seismogenic Fault in a Magmatic Arc: The Bolfin Fault Zone (Atacama Fault System). *Tectonics*, *40*(8). https://doi.org/10.1029/2021TC006818

McGarr, A. (2014). Maximum magnitude earthquakes induced by fluid injection. *Journal of Geophysical Research: Solid Earth*. https://doi.org/https://doi.org/10.1002/2013JB010597

Mesimeri, M., Pankow, K. L., Baker, B., & Hale, J. M. (2021). Episodic Earthquake Swarms in the Mineral Mountains, Utah Driven by the Roosevelt Hydrothermal System. *Journal of Geophysical Research: Solid Earth*, *126*(6). https://doi.org/10.1029/2021JB021659

Micklethwaite, S., & Cox, S. F. (2004). Fault-segment rupture, aftershock-zone fluid flow, and mineralization. *Geology*, *32*(9), 813–816. https://doi.org/https://doi.org/10.1130/G20559.1

Micklethwaite, S., Sheldon, H. A., & Baker, T. (2010). Active fault and shear processes and their implications for mineral deposit formation and discovery. *Journal of Structural Geology*, *32*(2), 151–165. https://doi.org/10.1016/j.jsg.2009.10.009

Mitchell, T. M., Ben-Zion, Y., & Shimamoto, T. (2011). Pulverized fault rocks and damage asymmetry along the Arima-Takatsuki Tectonic Line, Japan. *Earth and Planetary Science Letters*, *308*(3–4), 284–297. https://doi.org/10.1016/j.epsl.2011.04.023

Mittempergher, S., Dallai, L., Pennacchioni, G., Renard, F., & Di Toro, G. (2014). Origin of hydrous fluids at seismogenic depth: Constraints from natural and experimental fault rocks. *Earth and Planetary Science Letters*, *385*, 97–109. https://doi.org/10.1016/j.epsl.2013.10.027

Mogi, K. (1963). Some Discusions on Aftershocks, Foreshocks and Earthquake Swarms: The Fracture of a Semi-Infinite Body Caused by Inner Stress Origin and Its Relation to the Earthquake Phenomena (3rd Paper). *Bulletin of the Earthquake Research Institute*, *41*, 615–658.

Muñoz-Montecinos, J., Angiboust, S., Cambeses, A., & García-Casco, A. (2020). Multiple veining in a paleo–accretionary wedge: The metamorphic rock record of prograde dehydration and transient high pore-fluid pressures along the subduction interface (Western Series, central Chile). *Geosphere*, *16*(3), 765–786. https://doi.org/10.1130/GES02227.1

Okubo, K., Bhat, H. S., Rougier, E., Marty, S., Schubnel, A., Lei, Z., … Klinger, Y. (2019). Dynamics,

745 Radiation, and Overall Energy Budget of Earthquake Rupture With Coseismic Off-Fault Damage.
746 *Journal of Geophysical Research: Solid Earth*, *124*(11), 11771–11801.
747 https://doi.org/10.1029/2019JB017304

748 Ostermeijer, G. A., Aben, F. M., Mitchell, T. M., Rockwell, T. K., Rempe, M., & Farrington, K. (2022).
749 Evolution of co-seismic off-fault damage towards pulverisation. *Earth and Planetary Science*
750 *Letters*, *579*, 117353. https://doi.org/10.1016/j.epsl.2021.117353

751 Passarelli, L., Rivalta, E., Jónsson, S., Hensch, M., Metzger, S., Jakobsdóttir, S. S., … Dahm, T. (2018).
752 Scaling and spatial complementarity of tectonic earthquake swarms. *Earth and Planetary Science*
753 *Letters*, *482*, 62–70. https://doi.org/10.1016/j.epsl.2017.10.052

754 Petley-Ragan, A., Ben-Zion, Y., Austrheim, H., Ildefonse, B., Renard, F., & Jamtveit, B. (2019).
755 Dynamic earthquake rupture in the lower crust. *Science Advances*, *5*(7).
756 https://doi.org/10.1126/sciadv.aaw0913

757 Phillips, W. J. (1972). Hydraulic fracturing and mineralization. *Journal of the Geological Society*, *128*(4),
758 337–359. https://doi.org/10.1144/gsjgs.128.4.0337

759 Piana Agostinetti, N., Giacomuzzi, G., & Chiarabba, C. (2017). Seismic swarms and diffuse fracturing
760 within Triassic evaporites fed by deep degassing along the low-angle Alto Tiberina normal fault
761 (central Apennines, Italy). *Journal of Geophysical Research: Solid Earth*, *122*(1), 308–331.
762 https://doi.org/10.1002/2016JB013295

763 Poli, P., Cabrera, L., Flores, M. C., Báez, J. C., Ammirati, J. B., Vásquez, J., & Ruiz, S. (2021). Volcanic
764 Origin of a Long-Lived Swarm in the Central Bransfield Basin, Antarctica. *Geophysical Research*
765 *Letters*. https://doi.org/https://doi.org/10.1029/2021GL095447

766 Poli, P., Jeria, A. M., & Ruiz, S. (2017). The M w 8.3 Illapel earthquake (Chile): Preseismic and
767 postseismic activity associated with hydrated slab structures. *Geology*, *45*(3), 247–250.
768 https://doi.org/10.1130/G38522.1

769 Price, N. J., & Cosgrove, J. W. (1990). *Analysis of Geological Structures*. Cambridge University Press.
770 Reches, Z., & Dewers, T. (2005). Gouge formation by dynamic pulverization during earthquake rupture.
771 *Earth and Planetary Science Letters*, *235*(1–2), 361–374.
772 https://doi.org/10.1016/j.epsl.2005.04.009
773 Richards, J. P. (2013). Giant ore deposits formed by optimal alignments and combinations of geological
774 processes. *Nature Geoscience*, *6*(11), 911–916. https://doi.org/10.1038/ngeo1920
775 Ross, Z. E., & Cochran, E. S. (2021). Evidence for Latent Crustal Fluid Injection Transients in Southern
776 California From Long-Duration Earthquake Swarms. *Geophysical Research Letters*, *48*(12).
777 https://doi.org/10.1029/2021GL092465
778 Ross, Z. E., Cochran, E. S., Trugman, D. T., & Smith, J. D. (2020). 3D fault architecture controls the
779 dynamism of earthquake swarms. *Science*, *368*(6497), 1357–1361.
780 https://doi.org/10.1126/science.abb0779
781 Ross, Z. E., Hauksson, E., & Ben-Zion, Y. (2017). Abundant off-fault seismicity and orthogonal
782 structures in the San Jacinto fault zone. *Science Advances*, *3*(3), e1601946.
783 https://doi.org/10.1126/sciadv.1601946
784 Rutter, E. H., Maddock, R. H., Hall, S. H., & White, S. H. (1986). Comparative microstructures of natural
785 and experimentally produced clay-bearing fault gouges. *Pure and Applied Geophysics PAGEOPH*,
786 *124*(1–2), 3–30. https://doi.org/10.1007/BF00875717
787 Scheuber, E., & González, G. (1999). Tectonics of the Jurassic-Early Cretaceous magmatic arc of the
788 north Chilean Coastal Cordillera (22°-26°S): A story of crustal deformation along a convergent plate
789 boundary. *Tectonics*, *18*(5), 895–910. https://doi.org/10.1029/1999TC900024
790 Scholz, C. H. (2019). The Mechanics of Earthquakes and Faulting. In *The Mechanics of Earthquakes*
791 *and Faulting*. https://doi.org/10.1017/9781316681473
792 Seymour, N. M., Singleton, J. S., Gomila, R., Mavor, S. P., Heuser, G., Arancibia, G., … Stockli, D. F.

(2021). Magnitude, timing, and rate of slip along the Atacama fault system, northern Chile: implications for Early Cretaceous slip partitioning and plate convergence. *Journal of the Geological Society*, jgs2020-142. https://doi.org/10.1144/jgs2020-142

Shelly, D. R., Ellsworth, W. L., & Hill, D. P. (2016). Fluid-faulting evolution in high definition: Connecting fault structure and frequency-magnitude variations during the 2014 Long Valley Caldera, California, earthquake swarm. *Journal of Geophysical Research: Solid Earth*, *121*(3), 1776–1795. https://doi.org/10.1002/2015JB012719

Shelly, D. R., Hill, D. P., Massin, F., Farrell, J., Smith, R. B., & Taira, T. (2013). A fluid-driven earthquake swarm on the margin of the Yellowstone caldera. *Journal of Geophysical Research: Solid Earth*, *118*(9), 4872–4886. https://doi.org/10.1002/jgrb.50362

Shelly, D. R., Skoumal, R. J., & Hardebeck, J. L. (2022). Fracture-mesh faulting in the swarm-like 2020 Maacama sequence revealed by high-precision earthquake detection, location, and focal mechanisms. *Geophysical Research Letters*. https://doi.org/10.1029/2022GL101233

Shelly, D. R., Taira, T., Prejean, S. G., Hill, D. P., & Dreger, D. S. (2015). Fluid-faulting interactions: Fracture-mesh and fault-valve behavior in the February 2014 Mammoth Mountain, California, earthquake swarm. *Geophysical Research Letters*, *42*(14), 5803–5812. https://doi.org/10.1002/2015GL064325

Sibson, R. H. (1985). Stopping of earthquake ruptures at dilational fault jogs. *Nature*, *316*(6025), 248–251. https://doi.org/10.1038/316248a0

Sibson, R. H. (1989). Earthquake faulting as a structural process. *Journal of Structural Geology*, *11*(1–2), 1–14. https://doi.org/10.1016/0191-8141(89)90032-1

Sibson, R. H. (1992a). Fault-valve behavior and the hydrostatic-lithostatic fluid pressure interface. *Earth Science Reviews*, *32*(1–2), 141–144. https://doi.org/10.1016/0012-8252(92)90019-P

Sibson, R. H. (1992b). Implication of fault-valve behaviour for rupture nucleation and recurrence.

*Tectonophysics*, *211*, 283–293.

Sibson, R. H. (1996). Structural permeability of fluid-driven fault-fracture meshes. *Journal of Structural Geology*, *18*(8), 1031–1042. https://doi.org/10.1016/0191-8141(96)00032-6

Sibson, R. H. (2020). Preparation zones for large crustal earthquakes consequent on fault-valve action. *Earth, Planets and Space*, *72*(1), 31. https://doi.org/10.1186/s40623-020-01153-x

Smith, S. A. F., Collettini, C., & Holdsworth, R. E. (2008). Recognizing the seismic cycle along ancient faults: CO2-induced fluidization of breccias in the footwall of a sealing low-angle normal fault. *Journal of Structural Geology*, *30*(8), 1034–1046. https://doi.org/10.1016/j.jsg.2008.04.010

Stanton-Yonge, A., Cembrano, J., Griffith, W. A., Jensen, E., & Mitchell, T. M. (2020). Self-similar length-displacement scaling achieved by scale-dependent growth processes: Evidence from the Atacama Fault System. *Journal of Structural Geology*, *133*, 103993. https://doi.org/10.1016/j.jsg.2020.103993

Stierle, E., Bohnhoff, M., & Vavryčuk, V. (2014). Resolution of non-double-couple components in the seismic moment tensor using regional networks—II: application to aftershocks of the 1999 Mw 7.4 Izmit earthquake. *Geophysical Journal International*, *196*(3), 1878–1888. https://doi.org/10.1093/gji/ggt503

Sykes, L. R. (1978). Intraplate seismicity, reactivation of preexisting zones of weakness, alkaline magmatism, and other tectonism postdating continental fragmentation. *Reviews of Geophysics*, *16*(4), 621–688. https://doi.org/https://doi.org/10.1029/RG016i004p00621

Tardani, D., Reich, M., Roulleau, E., Takahata, N., Sano, Y., Pérez-Flores, P., … Arancibia, G. (2016). Exploring the structural controls on helium, nitrogen and carbon isotope signatures in hydrothermal fluids along an intra-arc fault system. *Geochimica et Cosmochimica Acta*, *184*, 193–211. https://doi.org/10.1016/j.gca.2016.04.031

Trepmann, C. A., & Stöckhert, B. (2003). Quartz microstructures developed during non-steady state

841 plastic flow at rapidly decaying stress and strain rate. *Journal of Structural Geology*, *25*(12), 2035–
842 2051. https://doi.org/10.1016/S0191-8141(03)00073-7
843 Trepmann, C. A., & Stöckhert, B. (2013). Short-wavelength undulatory extinction in quartz recording
844 coseismic deformation in the middle crust – an experimental study. *Solid Earth*, *4*(2), 263–276.
845 https://doi.org/10.5194/se-4-263-2013
846 Ujiie, K., Saishu, H., Fagereng, Å., Nishiyama, N., Otsubo, M., Masuyama, H., & Kagi, H. (2018). An
847 Explanation of Episodic Tremor and Slow Slip Constrained by Crack-Seal Veins and Viscous Shear
848 in Subduction Mélange. *Geophysical Research Letters*, *45*(11), 5371–5379.
849 https://doi.org/10.1029/2018GL078374
850 Vavryčuk, V. (2002). Non-double-couple earthquakes of 1997 January in West Bohemia, Czech
851 Republic: evidence of tensile faulting. *Geophysical Journal International*, *149*(2), 364–373.
852 https://doi.org/10.1046/j.1365-246X.2002.01654.x
853 Veloso, E. E., Gomila, R., Cembrano, J., González, R., Jensen, E., & Arancibia, G. (2015). Stress fields
854 recorded on large-scale strike-slip fault systems: Effects on the tectonic evolution of crustal slivers
855 during oblique subduction. *Tectonophysics*, *664*, 244–255.
856 https://doi.org/10.1016/j.tecto.2015.09.022
857 Vermilye, J. M., & Scholz, C. H. (1998). The process zone: a microstructural view of fault growth.
858 *Journal of Geophysical Research: Solid Earth*, *103*.
859 Vidale, J. E., & Shearer, P. M. (2006). A survey of 71 earthquake bursts across southern California:
860 Exploring the role of pore fluid pressure fluctuations and aseismic slip as drivers. *Journal of*
861 *Geophysical Research: Solid Earth*, *111*(B5), n/a-n/a. https://doi.org/10.1029/2005JB004034
862 Wells, D. L., & Coppersmith, K. J. (1994). New empirical relationships among magnitude, rupture
863 length, rupture width, rupture area, and surface displacement. *Bulletin of the Seismological Society*
864 *of America*, *84*(4), 974–1002. https://doi.org/https://doi.org/10.1785/BSSA0840040974

Wesnousky, S. G. (1988). Seismological and structural evolution of strike-slip faults. *Nature*, *335*(6188), 340–343. https://doi.org/10.1038/335340a0

Wesnousky, S. G. (2006). Predicting the endpoints of earthquake ruptures. *Nature*, *444*(7117), 358–360. https://doi.org/10.1038/nature05275

Wibberley, C. A. J., Yielding, G., & Di Toro, G. (2008). Recent advances in the understanding of fault zone internal structure: A review. *Geological Society Special Publication*, *299*, 5–33. https://doi.org/10.1144/SP299.2

Williams, R. T. (2019). Coseismic boiling cannot seal faults: Implications for the seismic cycle. *Geology*, *47*(5), 461–464. https://doi.org/10.1130/G45936.1

Williams, R. T., & Fagereng, Å. (2022). The Role of Quartz Cementation in the Seismic Cycle: A Critical Review. *Reviews of Geophysics*, *60*(1). https://doi.org/10.1029/2021RG000768

Yukutake, Y., Ito, H., Honda, R., Harada, M., Tanada, T., & Yoshida, A. (2011). Fluid-induced swarm earthquake sequence revealed by precisely determined hypocenters and focal mechanisms in the 2009 activity at Hakone volcano, Japan. *Journal of Geophysical Research*, *116*(B4), B04308. https://doi.org/10.1029/2010JB008036